The atomic hydrogen content of the post-reionization Universe

Marta Spinelli [1,2,3]★ Anna Zoldan [1] Gabriella De Lucia [1,3] Lizhi Xie[4]
and Matteo Viel[1,2,3,5]

[1]*INAF – Osservatorio Astronomico di Trieste, Via G.B. Tiepolo 11, I-34143 Trieste, Italy*
[2]*INFN, Sezione di Trieste, Via Valerio 2, I-34127 Trieste, TS, Italy*
[3]*IFPU – Institute for Fundamental Physics of the Universe, Via Beirut 2, I-34014 Trieste, Italy*
[4]*Tianjin Astrophysics Center, Tianjin Normal University, Binshuixidao 393, Tianjin 300384, China*
[5]*SISSA, International School for Advanced Studies, Via Bonomea 265, I-34136 Trieste, TS, Italy*

ABSTRACT

We present a comprehensive analysis of atomic hydrogen (H I) properties using a semi-analytical model of galaxy formation and *N*-body simulations covering a large cosmological volume at high resolution. We examine the H I mass function and the H I density, characterizing both their redshift evolution and their dependence on hosting halo mass. We analyse the H I content of dark matter haloes in the local Universe and up to redshift $z = 5$, discussing the contribution of different galaxy properties. We find that different assembly history plays a crucial role in the scatter of this relation. We propose new fitting functions useful for constructing mock H I maps with halo occupation distribution techniques. We investigate the H I clustering properties relevant for future 21 cm intensity mapping (IM) experiments, including the H I bias and the shot-noise level. The H I bias increases with redshift and it is roughly flat on the largest scales probed. The scale dependence is found at progressively larger scales with increasing redshift, apart from a dip feature at $z = 0$. The shot-noise values are consistent with the ones inferred by independent studies, confirming that shot noise will not be a limiting factor for IM experiments. We detail the contribution from various galaxy properties on the H I power spectrum and their relation to the halo bias. We find that H I poor satellite galaxies play an important role at the scales of the one-halo term. Finally, we present the 21 cm signal in redshift space, a fundamental prediction to be tested against data from future radio telescopes such as Square Kilometre Array.

Key words: methods: numerical – galaxies: evolution – galaxies: intergalactic medium – large-scale structure of Universe.

1 INTRODUCTION

In the attempt to unravel the mysteries of the dark Universe, mapping its large-scale structure on progressively larger volumes is crucially important. The ubiquitous cosmic neutral hydrogen (H I), seen through the 21 cm line, is one of the best candidates to illuminate the underlying dark matter density distribution. In the post-reionization Universe, most neutral hydrogen is expected to be in dense systems inside galaxies, like damped Lyman α absorbers, where the H I has been shielded from ionizing ultraviolet photons, thus tracing well the galaxy distribution (e.g. Furlanetto, Oh & Briggs 2006; Pritchard & Loeb 2010). The 21 cm redshifted signal (from the spin flip transition between the hyperfine states of the neutral hydrogen) therefore provides the possibility of performing tomographic studies

of cosmic structures. Using radio telescopes at frequencies between 1420 and 250 MHz, one can probe the 21cm line up to the end of the reionization epoch.

To observe the required large volumes within reasonable amounts of telescope time, one solution is to integrate the signal in large angular pixels of the sky, without resolving individual H I galaxies, whose signal is already faint ($\sim$ μJy) at $z \sim 1.5$. This relatively new technique, called intensity mapping (IM), can be used to probe the large-scale structure of the Universe, and constrain cosmology with competitive precision (e.g. Bharadwaj, Nath & Sethi 2001; Battye, Davies & Weller 2004; Chang et al. 2008; Loeb & Wythe 2008).

Although the measurement of the autopower spectrum of H I IM survey is currently challenged by the contamination from foreground residuals (Switzer et al. 2013), statistical detection of the signal has been achieved in cross-correlation: first measurements of the 21 cm IM signal have been obtained using the

★ E-mail: spinemart@gmail.com

Giant Meterwave Radio Telescope in cross-correlation with the DEEP2 optical redshift survey (Chang et al. 2010) and with the emission line galaxy redshift survey WiggleZ (Masui et al. 2013), and using the Parkes telescope in cross-correlation with the 2dF survey (Anderson et al. 2018). Several other surveys are already ongoing or have been proposed, such as the Canadian Hydrogen Intensity Mapping Experiment (Bandura et al. 2014), the Tianlai cylinder array (Xu, Wang & Chen 2015), the Hydrogen Intensity and Real-time Analysis eXperiment (Newburgh et al. 2016), and surveys using MeerKAT (Santos et al. 2017). Ultimately, the Square Kilometre Array (SKA), combining an SKA1-MID WideBand survey (20 000 deg² and 10 000 h integration time in single dish mode) with an SKA1-LOW deep-like survey (100 deg² sky coverage and 5000 h integration time), will provide a unique picture of H I on cosmological scales over a wide redshift range ($0 < z < 6$). While ultradeep radio continuum surveys planned on SKA will be crucial to characterize the statistical properties of the star-forming galaxy population and thus the coevolution between galaxies and supermassive black holes (e.g. Mancuso et al. 2017), IM surveys will have a great impact on cosmology. Indeed, the IM signal will constrain the expansion history of the Universe and the growth of structures, allowing us to measure neutrino masses (Villaescusa-Navarro, Bull & Viel 2015), to test dark matter nature at small scales (Carucci et al. 2015), to look for signatures of inflation in the power spectrum (Xu, Hamann & Chen 2016; Ballardini et al. 2018), and to probe the geometry of the Universe with baryon acoustic oscillations (BAOs; Bull et al. 2015; Villaescusa-Navarro, Alonso & Viel 2017).

The primary tool adopted to describe the distribution of atomic hydrogen in the Universe is the 21 cm power spectrum $P_{21cm}(k, z)$ that is a function of scale k and of redshift. In redshift space, matter peculiar velocities result in an apparent enhancement of clustering on large scales (Kaiser 1987), and the signal can be modelled as

$$P_{21cm}(z, k) = T_b^2 \left[\left(b_{HI(k)}^2 + f \mu_k^2 \right)^2 P_m(z, k) + P_{SN} \right] , \quad (1)$$

where T_b is the mean brightness temperature that depends on the cosmic density of neutral hydrogen $\rho_{HI}(z)$, $b_{HI}(k)$ is the H I bias, f is the linear growth rate, $\mu_k = \hat{k} \cdot \hat{z}$, $P_m(z, k)$ is the linear matter power spectrum, and P_{SN} is the H I shot noise. In real space, there is a degeneracy between $\rho_{HI}(z)$ and the H I bias that can be broken using redshift space distortion (RSD; Masui et al. 2013). The IM signal can be completely specified knowing the H I density, the bias, and the shot noise. An accurate modelling of these quantities is thus crucial in the preparation of future survey data exploitation.

A convenient and fast approach to model the H I distribution on large scales is to use halo occupation distribution (HOD) techniques. In these methods, the H I content of dark matter haloes depends only on halo mass – this defines the H I halo mass function $M_{HI}(M_h)$ – and all the quantities described above can be related to this quantity (e.g. Santos et al. 2015; Villaescusa-Navarro et al. 2018). Halo catalogues obtained with approximate methods such as Lagrangian perturbation theory (e.g. Monaco, Theuns & Taffoni 2002) can be used to populate the dark matter haloes with H I, in combination with parametrizations for the H I halo mass function. This allows the creation of a large number of H I mock catalogues, with relatively small computational resources. Standard HOD approaches, however, do not model the spatial distribution of H I within dark matter haloes and generally neglect possible environmental dependences and assembly bias (e.g. Gao & White 2007). This can have important consequences when using this approach to carry out precision cosmology experiments.

An alternative approach to model the H I distribution in a cosmological context is based on hydrodynamical simulations (e.g. Duffy et al. 2012; Davé et al. 2013; Zavala et al. 2016; Villaescusa-Navarro et al. 2018). Physical processes like star formation, feedback from stellar winds, supernovae and active galactic nuclei (AGNs), black hole accretion, etc. are included using 'sub-grid' models, while the approach allows an explicit and self-consistent treatment of the gas dynamics. From the computational point of view, large high-resolution simulations require large investment of resources. In addition, a self-consistent modelling of the H I content is not typically accounted for as it would require, in principle, a consistent treatment of the formation of molecular hydrogen on dust grains, and of the transition from molecular to atomic hydrogen including a proper treatment for photodissociation and self-shielding. Therefore, H I is usually computed in post-processing (e.g. Duffy et al. 2012; Lagos et al. 2015). An independent and more efficient approach is provided by semi-analytical models (SAMs) of galaxy formation, coupled to merger trees extracted from high-resolution *N*-body simulations. In this case, the advantage is a significantly reduced computational cost and the access to a large dynamic range in mass and spatial resolution. The physical processes driving the evolution of the baryonic components of dark matter haloes are included using simple yet physically and/or observational motivated prescriptions that are equivalent to the sub-grid modelling used in hydrodynamical simulations (in fact, often some prescriptions are constructed using controlled numerical experiments). The most recent renditions of several independent SAMs have included prescriptions to partition the cold gas in its atomic and molecular components, based either on empirical relations or on results from sophisticated numerical simulations (e.g. Fu et al. 2010; Kim et al. 2011; Lagos et al. 2011; Somerville & Davé 2015; Stevens et al. 2017; Xie et al. 2017; Zoldan et al. 2017; Cora et al. 2018). These models can provide reliable mock 21 cm maps, thereby helping to understand the relevant processes determining the observed 21 cm signal.

In this paper, we take advantage of the state-of-the-art SAM GAlaxy Evolution and Assembly (GAEA), whose relevant features/details are described in Section 2. In Section 3, we analyse the H I mass function both as a function of halo mass (Section 3.1) and as a function of redshift (Section 3.2). In Section 4, we discuss the H I density, while we investigate the H I content of dark matter haloes in Section 5 focusing in particular on the halo H I mass function ($M_{HI}(M_h)$, Section 5.1) and on the shape of the H I profile (Section 5.2). What we learn from this analysis helps understanding the clustering signal of neutral hydrogen (Section 6). We discuss both shot noise and the H I bias (in Sections 6.1 and 6.2, respectively) and how the clustering signal varies as a function of halo mass (Section 6.3), galaxy type (Section 6.4), H I mass (Section 6.5), and colour (Section 6.6). In Section 6.7, we discuss the effect of the RSD on the H I power spectrum, and give our predictions for the 21 cm signal. We draw conclusions in Section 7.

2 SIMULATIONS

This work is based on outputs from the GAEA SAM. The model and all its upgrades are described in details in several papers (e.g. De Lucia et al. 2014; Hirschmann, De Lucia & Fontanot 2016; Xie et al. 2017; Zoldan et al. 2017). We summarize here the main features that are relevant for the analysis presented in this paper.

GAEA has been run on the merger trees of two large-scale dark matter cosmological simulations: the Millennium I (MI) simulation (Springel et al. 2005) and the Millennium II (MII) simulation

Table 1. Main parameters of the simulations used in this study: number of particles N_p, comoving box size ℓ_{box}, and minimum resolved mass of dark matter substructures $\min(M_h)$. In the last column, we give the minimum stellar mass $\min(M_s)$ that we consider in this analysis.

Simulation	N_p	ℓ_{box} $(h^{-1}\,\mathrm{Mpc})$	$\min(M_h)$ $(h^{-1}\,\mathrm{M_\odot})$	$\min(M_s)$ $(h^{-1}\,\mathrm{M_\odot})$
MI	2160^3	500	1.7×10^{10}	10^8
MII	2160^3	100	1.4×10^8	10^6

(Boylan-Kolchin et al. 2009). While the latter has a better mass resolution, the former covers a larger volume. The main parameters of the simulations are listed in Table 1. Both simulations are based on a *WMAP*1 cosmological model (Spergel et al. 2003) with $\Omega_m = 0.25$, $\Omega_b = 0.045$, $h = 0.73$, and $\sigma_8 = 0.9$. Although latest *Planck* measurements (Planck Collaboration XIII 2016; Planck Collaboration VI 2018) point towards a lower value for σ_8, and a higher value of Ω_m, these differences are not expected to have a major impact on the predictions from our SAMs (Wang et al. 2008; Guo et al. 2013).

The SUBFIND algorithm (Springel et al. 2001) has been used to identify bound substructures (subhaloes) within standard Friend-of-Friend (FoF) dark matter haloes. The bound part of the FoF group represents what is referred to as the 'main subhalo', and hosts the central galaxy, while satellite galaxies are associated with all other bound subhaloes. Merger trees are constructed identifying a unique descendant for each subhalo, by tracing the majority of the most bound particles. When a halo is accreted on to a more massive system (i.e. it becomes a substructure), it suffers significant stripping by tidal interaction. In particular, it can be stripped below the resolution of the dark matter simulation, when still at a significant distance from the parent halo centre, i.e. when the merger between the galaxy it hosts and the central galaxy is incomplete. The SAM accounts for this by introducing 'orphan' galaxies (Type II in our jargon versus Type I that are associated with distinct dark matter substructures). The evolution of these galaxies is traced by following the most bound particle of the parent substructure before it disappeared, and the galaxy is assigned a residual merger time that is given by a variation of the dynamical friction formula (De Lucia & Blaizot 2007; De Lucia et al. 2010).

The GAEA SAM follows the evolution of the different baryonic components of model galaxies. Different reservoirs are considered: the stars in the bulge and in the disc, the cold gas in the galactic disc, a diffuse hot gas component, and an ejected gas component both associated with the parent dark matter haloes. The model has prescriptions for the transfer of mass, metals, and energy between these different components, including gas cooling, star formation, and stellar feedback. When a halo is identified for the first time, it is assigned a hot gas reservoir that is proportional to its dark matter mass (via the universal baryon fraction). This gas can then cool on to the galactic disc of the central galaxy either via a 'rapid' or a 'slow' accretion mode. The cooling is 'rapid' if the characteristic cooling radius, which depends mainly on the temperature and the metallicity of the gas, is larger than the halo virial radius, and 'slow' otherwise. Generally, gas cooling is rapid for small haloes at early epochs, and becomes slower for more massive haloes and at lower redshift.

The collapse of the cold gas leads to the formation of stars. Observations have shown that there is a strong correlation between the surface density of the molecular gas and that of star formation,

against no significant correlation between H I content and star formation (e.g. Wong & Blitz 2002; Kennicutt et al. 2007; Leroy et al. 2008). This is accounted for in the GAEA model through an explicit dependence of star formation on the molecular gas content (Xie et al. 2017). At each time-step, the galactic disc is divided into concentric rings and, in the model version we are using, the cold gas is partitioned into atomic (H I) and molecular (H₂) gas using an empirical power-law relation: $H_2/H_I = (P_{ext}/P_0)^\alpha$ between the molecular to atomic ratio (H₂/H I) and the hydrostatic mid-plane pressure of the disc (P_{ext}; Blitz & Rosolowsky 2006). The index α and the pivot scale P_0 are tuned to observational data in the local Universe. In each ring, the star formation rate density is assumed to be proportional to the molecular hydrogen surface density, and the total star formation rate is obtained summing the contributions from all rings. A star formation efficiency parameter regulates how much H₂ is converted into stars, and its value is tuned to reproduce the observed H I mass function in the local Universe (see Section 3). Our H₂ based star formation law predicts an increasing molecular fraction with increasing redshift, in qualitative agreement with what inferred from observational data (see also discussion in Popping et al. 2015). With respect to the case of fixed molecular fraction, this lowers the number density for H I-rich galaxies at high redshift. Moreover, the molecular fraction depends on stellar mass, which also disproves the idea of a fixed molecular fraction. The version of GAEA used in this work reproduces well the measured galaxy stellar mass function up to $z \sim 3$, and there is also a remarkable agreement between model predictions and the observed scaling relations between H I and H₂ masses and the galaxy stellar mass (Xie et al. 2017).

The model also includes a treatment for specific angular momentum exchanges between different components (Xie et al. 2017). In particular, the hot gas halo is assumed to have the same specific angular momentum of the parent halo. This specific angular momentum is transferred to the cold gas disc proportionally to the cooled mass, and then to the stellar disc proportionally to the mass of formed stars. The specific angular momentum of a disc is used to consistently estimate its scale radius that is proportional to the angular momentum divided by the circular velocity of the halo (at the time of accretion for satellite galaxies).

At the end of their life-cycle, stars eject mass, energy, and metals through winds or supernovae explosions. These stellar feedback events are assumed to reheat the cold gas of the disc and to eject part of the gas outside the galaxy parent halo. Reheated and ejected gas are both assigned to the reservoir of the central galaxy of each halo, even if coming from satellites. The gas can be re-accreted on to the central galaxy on time-scales inversely proportional to the virial mass of the halo (Henriques et al. 2013; Hirschmann et al. 2016). The GAEA model also includes a complex treatment of chemical enrichment, accounting for the non-instantaneous recycling of gas, metals and energy from Asymptotic Giant Branch stars, supernovae Type Ia and supernovae Type II. The model also includes a treatment for black holes and AGN feedback. At high redshift, black hole mass seeds are placed at the centre of haloes with virial temperature above 10^4 K. The seed mass scales with that of the parent haloes and ranges from 10^3 to 10^5 $M_\odot$ in the MI, and from 10 to 10^4 $M_\odot$ in the MII. Note that the different values for the seeds in the MI and MII are due to their different resolution. Black holes then grow through mergers (quasar mode) and hot gas accretion (radio mode). The latter is implemented in GAEA following Croton et al. (2006), thus relating the growth of a black hole to its mass, the virial velocity of the parent halo, and hot gas fraction. Accretion of gas from the hot gas atmosphere associated with dark matter haloes

generates a mechanical energy that reduces the cooling rate. This effect is important to suppress the H I content of massive haloes. Finally, in case of a merger event, the cold gas of the secondary galaxy (that is always a Type II) is added to the total cold gas disc of the primary (that can be a Type I or a central) and a starburst is triggered, with the new stars remaining in the disc of the remnant (Somerville, Primack & Faber 2001; Cox et al. 2008). Depending on the masses of the galaxies involved, the merging event can be considered a major or a minor event. In case of a major event, all stars (including the new ones) are moved to a spheroidal bulge.

3 THE H I MASS FUNCTION

In this section, we discuss the H I mass function (HIMF), i.e. the number density of galaxies with different H I mass, in the MI and MII simulations, focusing in particular on the role of central and satellite galaxies. In Section 3.1, we analyse the H I conditional mass function and its dependence on hosting halo mass, while in Section 3.2 we study the H I mass evolution with redshift. As discussed in Section 2, the star formation efficiency is tuned to reproduce the local Universe H I mass function measured by Zwaan et al. (2005) and Martin et al. (2010), using the blind H I surveys HIPASS (Meyer et al. 2004) and ALFALFA (Giovanelli et al. 2005), limited to redshifts $z < 0.04$ and $z < 0.06$, respectively. The agreement is very good, by construction, down to the smallest H I masses that are well resolved by our model applied to the MI and MII simulations. To avoid including unresolved galaxies, we apply a stellar mass cut that is evaluated, for the MII, on the basis of the good agreement between the predicted and observed stellar mass function (Baldry et al. 2012; Moustakas et al. 2013), down to a certain stellar mass threshold. In this work, we adopt a mass threshold of $M_s > 10^6 \, M_\odot$, although the stellar mass function of the model overpredicts the number of galaxies with $M_s \lesssim 10^{7.5} \, M_\odot$ of ~ 0.5 dex. For the MI, the stellar mass cut is based on the convergence with the higher resolution simulation: we find good agreement between MI and MII down to $M_s \sim 10^8 \, M_\odot$. We report the values of the cuts in Table 1. Previous work based on the GAEA model (e.g. Xie et al. 2017; Zoldan et al. 2017) adopted more conservative stellar mass limits ($\sim 10^9 \, M_\odot$ for the MI, and $\sim 10^8 \, M_\odot$ for the MII). In this work, we lower the stellar mass thresholds in order to access lower H I masses, as the minimum H I available is connected to the stellar mass selection. Indeed, Kim et al. (2017) show that low H I mass galaxies play a key role for the clustering signal, and therefore for the IM measurements we are interested in. As the measured H I mass function is well reproduced by our model, we do not expect the overestimation of the stellar mass function in the low mass end to influence our results.

In Fig. 1, we show the H I mass function for the MI and MII simulations at redshift zero. As discussed above, the model has been tuned to reproduce this quantity. Below $\sim 10^8 \, h^{-1} \, M_\odot$ the MI starts deviating from the MII, due to its resolution limits. Predictions from the MII follow rather well the observational measurements down to H I masses $\sim 10^7 \, h^{-1} \, M_\odot$.

While the agreement between our model predictions and observational data is not entirely surprising, we note that other models are characterized by an excess of galaxies at low H I masses. For example, the GALFORM model overpredicts by a factor 3 the H I number density around $\sim 10^8 \, h^{-1} \, M_\odot$ (e.g. Baugh et al. 2019). The excess is ascribed to halo mass resolution and to the implementation adopted for photoionization feedback (Kim et al. 2015). In the model presented by Popping et al. (2015), there is a similar excess due to low-mass galaxies ($M_s < 10^7 \, M_\odot$) residing in low-mass haloes
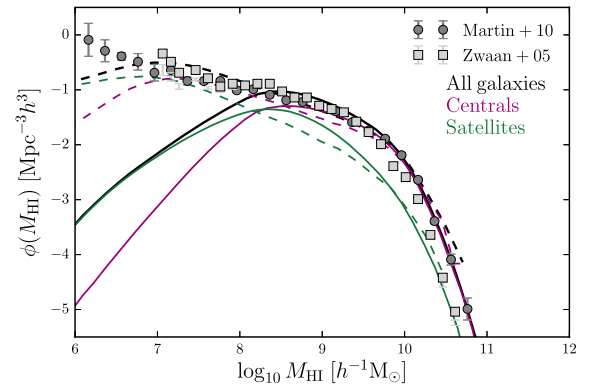

Figure 1. The H I mass function, i.e. the number density of galaxies with different H I mass, in the Millennium I (solid lines) and Millennium II (dashed lines) simulation at redshift zero. Magenta and green lines are used for centrals and satellites, respectively, while black lines are for all galaxies. Squares and circles with error bars show the data measured by Zwaan et al. (2005) and Martin et al. (2010) using the blind H I surveys HIPASS (Meyer et al. 2004, limited to $z < 0.04$) and ALFALFA (Giovanelli et al. 2005, limited to $z < 0.06$). In this work, we use $M_s > 10^8 \, M_\odot$ for the MI and $M_s > 10^6 \, M_\odot$ for the MII, as a compromise between resolution requirements and the inclusion of low H I mass galaxies in our sample.

($M_h < 10^{10} \, M_\odot$). This excess (or the lack of the excess in our model) has important consequences on the model predictions that we will discuss in the following sections.

In Fig. 1, we further separate the contribution from central and satellite galaxies. At the low-mass end of the HIMF satellite galaxies become increasingly important, starting from $M_{HI} \sim 10^8 \, h^{-1} \, M_\odot$ for the MI, and from $M_{HI} \sim 10^7 \, h^{-1} \, M_\odot$ for the MII. Lagos et al. (2011) argue that, in their model, central galaxies do not contribute much in this mass range because of the reionization scheme adopted: hot gas in small haloes is not allowed to cool, thus there is less H I in centrals. In contrast, satellites have formed before reionization, and therefore before this effect becomes efficient. For intermediate and high H I masses, the HIMF is dominated by central galaxies. This behaviour (i.e. central galaxies being more important at medium at high masses and satellites at small masses) is quite general and found also in other models (e.g. GALFORM; Kim et al.2017).

3.1 The H I conditional mass function

Fig. 2 shows the contribution to the H I mass function of galaxies hosted by haloes of different mass at $z = 0$. We show the same figure at $z = 4$ in Appendix A. As above, we further separate the contribution from central and satellite galaxies.

The conditional H I mass function emerges from a non-trivial convolution of the halo number density, baryon fraction, and gas cooling. The high-mass end of the H I mass function is dominated by H I in central galaxies hosted by massive haloes ($10^{12} < M_h[h^{-1} \, M_\odot] < 10^{14}$), in both the MI and MII. Just below the knee, in the mass range $10^8 < M_{HI}(h^{-1} \, M_\odot) < 10^{10}$, the main contributors are central galaxies in lower mass haloes ($10^{10} < M_h[h^{-1} \, M_\odot] < 10^{12}$), with satellite galaxies in haloes with mass $10^{12} < M_h[h^{-1} \, M_\odot] < 10^{14}$ also giving a non-negligible contribution. The lower mass end of the H I mass function is dominated by these satellite galaxies, with contributions from satellites in less (more) massive haloes for the MI (MII). Centrals from the lowest mass haloes are also important at these low masses, as also found by
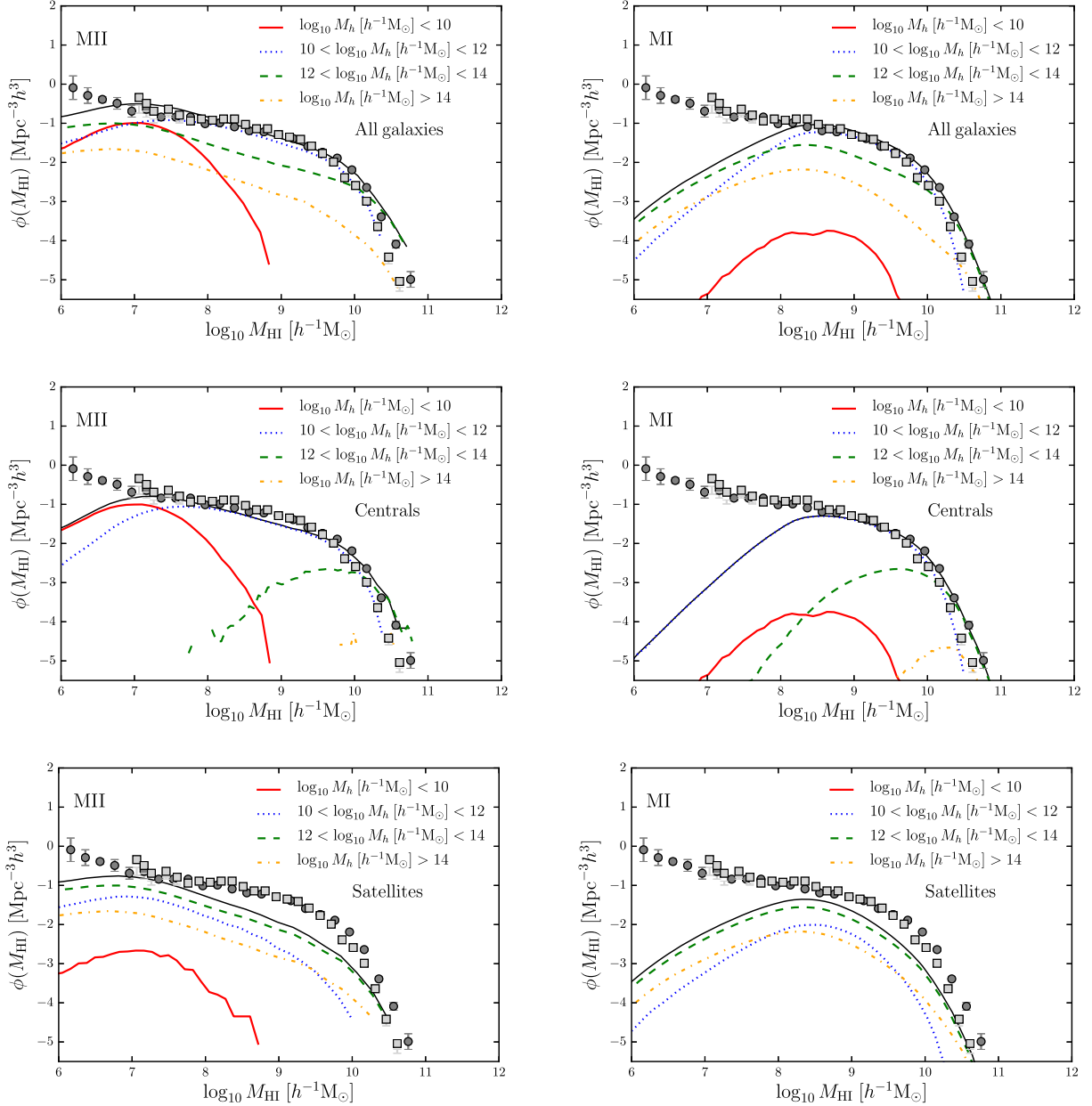
Figure 2. The predicted H I conditional mass function for the MII (left column) and the MI (right column). In the middle and bottom panels, we separate the contribution from central and satellite galaxies, respectively. The solid black line in each panel is the sum of the contributions from different host dark matter haloes. Squares and circles with error bars show observational measurements by Zwaan et al. (2005) and Martin et al. (2010) in the local Universe.

Popping et al. (2015). In the MII, the dominant contribution comes from the smallest haloes ($M_h < 10^{10} \, h^{-1} \, M_\odot$); in the MI case, these haloes are not resolved and the main contribution comes from the haloes with larger mass ($10^{10} < M_h[h^{-1} \, M_\odot] < 10^{12}$).

3.2 Redshift evolution of the H I mass function

In Fig. 3, we show the evolution of the H I mass function in the redshift range $0 < z < 5$. The high-mass end grows with decreasing redshift until $z \sim 1$, tracing the formation of progressively more massive haloes. At $z = 0$, the suppression of gas cooling due to AGN feedback (see Section 2) reverses slightly this trend. In the H I mass range $10^8 < M_{HI}[h^{-1} \, M_\odot] < 10^{10}$, where the H I mass function is

dominated by central galaxies in much lower mass haloes (where AGN feedback is not efficient), the number density of galaxies is largest at $z = 0$.

As for the $z = 0$ case discussed earlier, the resolution does not affect significantly the number density of galaxies with H I mass above $\sim 10^8 \, h^{-1} \, M_\odot$ in the MI, although this limit deteriorates slightly with increasing redshift, reaching $\sim 10^{8.5} \, h^{-1} \, M_\odot$ at $z = 5$. Below $\sim 10^8 \, h^{-1} \, M_\odot$, our model predicts a mild dependence on redshift for the global population and a stronger evolution for satellite galaxies, whose number is expected to increase with decreasing redshift. As discussed above, other models tend to overpredict the number density of galaxies with H I masses in the range $10^7 \lesssim M_{HI}[h^{-1} \, M_\odot] \lesssim 10^9$ at $z = 0$. This excess becomes more prominent and shifts
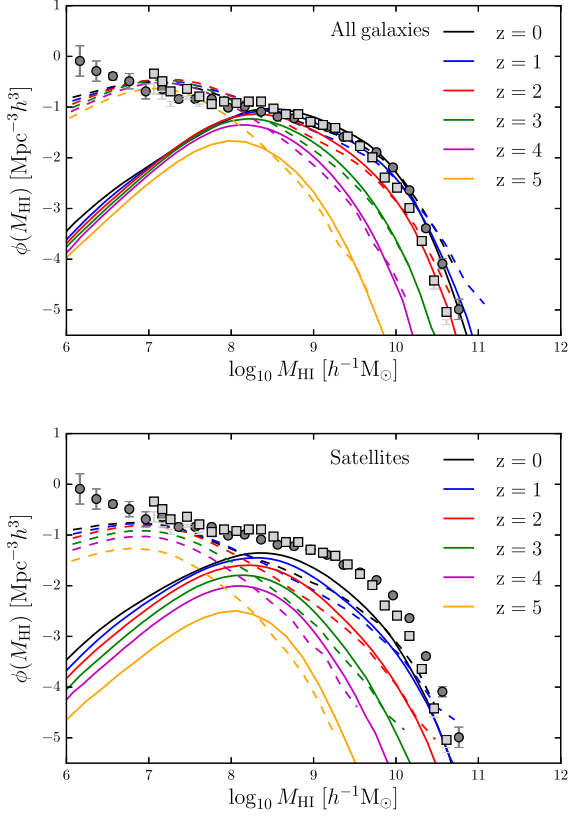
Figure 4. Evolution with redshift of the H I density $\rho_{H I}/\rho_{c,z=0}$ for the MI (thin lines) and MII (thick lines), divided into the contributions for different host dark matter halo masses. Differences between the two simulations can be appreciated only for very high and very low mass haloes. The GAEA model prediction are compared with observational data (Crighton et al. 2015, and references therein).

At high redshift, the observational measurements are based on damped Lyman α systems (DLAs) identified in the spectra of bright quasars. Although the physical origin of these systems is still debated (e.g. Pontzen et al. 2008; Tescari et al. 2009; Rahmati et al. 2013; Berry et al. 2014), the measurements based on DLAs are robust as they are relatively easy to identify in quasar spectra thanks to their prominent damping wings. The local and high-redshift measurements are, however, based on different strategies (emission and absorption, respectively). In the next future, thanks to the next generation of radio telescopes like SKA, we will be able to measure H I masses using both strategies for the same objects. At the moment, these two estimates are independent, and cannot exclude possible biases/systematics.

As discussed in Section 3.2, the H I mass function in our model does not evolve significantly with redshift for $M_{H I} < 10^8 \, h^{-1} \, M_\odot$, while independent models tend to predict larger number densities for low H I masses at higher redshift (see e.g. figs 7 and 12 in Popping, Somerville & Trager 2014, fig. 4 in Baugh et al. 2019, or figs 7 and 9 in Davé et al. 2017). These enhanced number densities clearly play a key role in the final H I content as a function of redshift, explaining in part the origin of the disagreement between our model predictions and observational data. In addition, the cosmic H I density depends significantly on the resolution of the simulations used. To emphasize this, in Fig. 4, we show the contribution to the total H I density from haloes of different mass. We show results for both the MI and the MII; the two simulations exhibit the same trends for haloes of intermediate and large mass, deviating only for cluster mass haloes ($M_h > 10^{14} \, h^{-1} \, M_\odot$) that are rare in the smaller volume of the MII simulation. The most evident difference is, as expected, for the smallest haloes, that start collapsing earlier than their larger mass counter-parts. Above $z \sim 5$, haloes smaller than $\sim 10^{10} \, h^{-1} \, M_\odot$ represent an important contribution to the cosmic number density of H I. These are resolved in the MII, while below the resolution limit of the MI simulation. We could partially fix the decreasing trend of H I with redshift, by assuming that the missing H I is contained in small, unresolved haloes. However, this solution would not be physically motivated and rather unrealistic, as these haloes should contain excessively large quantities of H I. We have verified that, extending our model predictions to halo masses of $10^7 \, h^{-1} \, M_\odot$, using the H I–halo mass relation predicted by our model and the Sheth & Tormen (1999) halo mass function, the maximum fractional

Figure 3. *Top panel*: The predicted H I mass function as a function of redshift for the MI (solid lines) and the MII simulation (dashed lines). *Bottom panel*: Contribution from satellite galaxies. For reference, we show with squares and circles the observational measurements of the H I mass function in the local Universe by Zwaan et al. (2005) and Martin et al. (2010), as in Fig. 1.

towards lower H I mass values with increasing redshift (e.g. Lagos et al. 2011; Davé et al. 2017; Baugh et al. 2019). It is difficult to understand the origin of the different behaviour between GAEA and independent models, as it likely originates from the complex and non-linear interaction between different physical processes implemented (in particular, photoionization feedback, star formation, and stellar feedback). Future observational programs that will allow the H I mass function to be measured beyond the local Universe, will provide important constraints on the model predictions discussed here.

4 H I DENSITY

In Fig. 4, we show the abundance of neutral hydrogen $\rho_{H I}(z)/\rho_{c,z=0}$ for the MI and MII simulations, as a function of redshift. Our results are tuned to agree with ALFALFA and HIPASS measurements at $z \sim 0$ (see also Fig. 1). At higher redshift, our model predicts a clear decrease of $\rho_{H I}(z)$ with respect to the observational data. This behaviour is shared by independent SAMs (e.g. Lagos et al. 2014) that, however, typically start from a larger value of the H I density at $z = 0$. The choice for this normalization is somewhat arbitrary, and driven by the ability/constraint to reproduce the observed H I mass function in the local Universe, and does not affect the trend for a decreasing cosmic H I density at higher redshift. Hydrodynamical simulations generally predict an opposite trend or significantly weaker evolution (e.g. Davé et al. 2017; Villaescusa-Navarro et al. 2018).
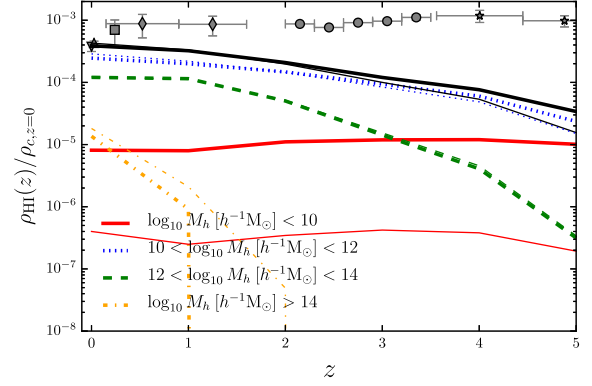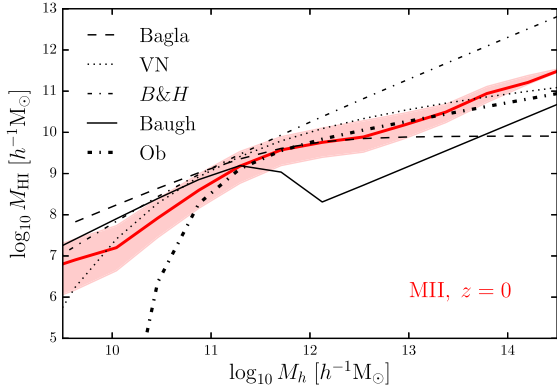
Figure 5. The median H I content of dark matter haloes in the MII simulation as a function of halo mass (red), at $z = 0$. The relation is compared to different parametrizations that have been introduced in the recent literature: Bagla et al. (2010, dashed), Villaescusa-Navarro et al. (2018, dotted), Barnes & Haehnelt (2010, thin dash–dotted); Baugh et al. (2019, solid), and Obuljen et al. (2019, thick dash–dotted). The red shaded area shows the 16th and 84th percentiles of the model distribution.

increase obtained for the cosmic H I density is of a factor ∼2 at $z \sim 5$. Even this very conservative calculation, that does not account properly for the effects of cosmic reionization, would be insufficient to obtain a better agreement with measurements based on DLAs. In summary, although resolution plays a role in the H I density determination, it seem unlikely that it is the main driver of the discrepancy with observational data.

A more subtle point, that deserves further investigations, is related to the adopted modelling of the reionization process. This is responsible for reducing the gas fraction in low-mass haloes below a characteristic mass that is redshift dependent and whose value, in our model, is based on results from hydrodynamical simulations (Gnedin 2000). Updating this model in the light of the late and fast reionization suggested by Planck data (Planck Collaboration VI 2018) could have an important effect on the H I cosmic density in the post-reionization era. Finally, it is important to stress that a decreasing H I density at higher redshift is in part expected because an increasing fraction of gas is expected to reside 'outside' haloes, in filaments and in the intergalactic medium. For example, studies based on hydrodynamical simulations (Villaescusa-Navarro et al. 2018) predict that the total H I inside haloes account only for 80 per cent of the total H I at $z \sim 5$.

5 H I CONTENT IN DARK MATTER HALOES

A detailed characterization of the H I content of dark matter haloes is a fundamental ingredient to make predictions for the 21 cm signal. This is particularly relevant for IM, especially in the framework of the halo model (Castorina & Villaescusa-Navarro 2017; Villaescusa-Navarro et al. 2018). Hydrodynamical simulations and SAMs are not only a valuable tool to model the relation between H I and halo mass, but also offer the possibility of investigating the physical origin of this relation. In this section, we analyse the H I halo mass function $M_{H I}(M_h)$ (Section 5.1) and its redshift evolution in the post-reionization Universe. We provide a fitting formula for it, discuss the different contributions from centrals and satellites, and the dependence on the assembly history of dark matter haloes. In Section 5.2, we focus on the H I spatial distribution within dark matter haloes, analysing the contribution from different satellite types.

Table 2. Best-fitting values for the parameters of the H I halo mass function $M_{H I}(M_h)$ parametrized in equation (2), at different redshifts.

z	a_1	a_2	α	β	$\log_{10}(M_{break})$ $(h^{-1}\,M_\odot)$	$\log_{10}(M_{min})$ $(h^{-1}\,M_\odot)$
0	0.42	8.7e−4	−3.7e−05	−0.70	12.1	11.4
1	3.8e−3	1.6e−3	0.24	1.70	8.30	−1.3
2	5.8e−4	1.5e−3	0.52	0.63	11.66	−3.11
3	1.7e−3	4.4e−4	0.47	0.23	12.30	−2.23
4	1.7e−3	3.4e−4	0.55	0.19	12.26	−2.75
5	5.2e−3	−5.5e−4	0.050	0.04	12.20	−3.71

5.1 The H I halo mass function

In this section, we analyse the average H I mass $M_{H I}$ hosted by a halo of mass M_h at redshift z; this represents the so-called H I halo mass function, $M_{H I}(M_h, z)$. Empirical models have been proposed for this relation by many authors (e.g. Bagla, Khandai & Datta 2010; Barnes & Haehnelt 2010; Santos et al. 2015; Padmanabhan, Refregier & Amara 2017; Villaescusa-Navarro et al. 2018; Baugh et al. 2019; Obuljen et al. 2019). The expectation is a linear relation between halo mass and H I mass, at least above a certain mass threshold. Due to different astrophysical processes like tidal stripping and photoionization, low-mass haloes are not expected to host large amounts of H I. Therefore, most parametrizations account for a cut-off at low masses. In Fig. 5, we show the $M_{H I}(M_h)$ at $z = 0$, estimated from our higher resolution simulation (i.e. MII), compared to other models that have been proposed and used in the recent literature. For halo masses $M_h > 10^{12.5}\,h^{-1}\,M_\odot$, the slope of the predicted relation becomes somewhat flatter than for lower mass haloes. This coincides with the significant 'dip' that has been reported by Baugh et al. (2019), and corresponds to the halo mass where AGN feedback becomes efficient. This behaviour is not described by a simple power-law model at high halo masses, that is instead typical of most parametrizations (see Fig. 5). For halo masses in the range $10^{10} < M_h < 10^{11.5}\,h^{-1}\,M_\odot$, the H I content drops. This physically motivated trend is shared by most parametrizations although the rate is different: some models predict almost no H I in small haloes (see Obuljen et al. 2019, in the figure), while other models have a smoother decline (see Barnes & Haehnelt 2010, in the figure). In this low-mass range, Bagla et al. (2010) have a cut-off at an even smaller mass (note however that the value in the figure is that at $z \sim 3$, but the authors speculate a shift to higher values at lower redshift), while Baugh et al. (2019) do not parametrize any cut-off. To fit our model predictions, we extend the parametrization by Baugh et al. (2019) to include a cut-off at low masses:

$$M_{H I}(M_h) = M_h \left[a_1 \left(\frac{M_h}{10^{10}} \right)^\beta e^{-\left(\frac{M_h}{M_{break}} \right)^\alpha} + a_2 \right] e^{-\left(\frac{M_{min}}{M_h} \right)^\gamma}, \quad (2)$$

where a_1, β, α, M_{break}, a_2, and M_{min} are free parameters. The value of γ is kept fixed to 0.5, which we find provides the best description of our model predictions, and is half way between 1 (the most common choice in literature) and the 0.35 adopted recently by Villaescusa-Navarro et al. (2018). The parametrization proposed assumes that the H I mass is proportional to the halo mass M_h at the high-mass end, and proportional to $M_h^{1+\beta}$ for intermediate masses. We list the best-fitting values of the free parameters that we find for our model predictions in Table 2. At $z = 0$, the value of M_{break} is $\sim 10^{12}\,h^{-1}\,M_\odot$, slightly larger than that reported in Baugh et al. (2019), in agreement with what we see in Fig. 5. The value of β is negative, which reflects the fact that the H I mass increases more slowly for intermediate-mass haloes than for the most massive ones. M_{min} is $10^{11.4}\,h^{-1}\,M_\odot$,
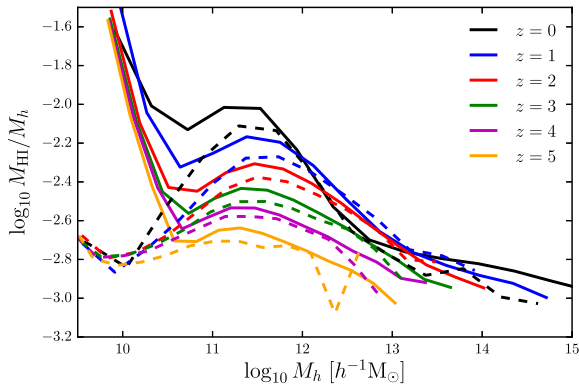
Figure 6. The fraction M_{HI}/M_h as a function of M_h, measured from the MI (solid lines) and the MII simulations (dashed lines), as a function of redshift (different colours).

Figure 7. The median H I content of dark matter haloes for the MI (solid lines) and for the MII simulations (dashed lines) as a function of halo mass, for central galaxies (violet) and satellites (green). We report the results for redshift 0, 1, 2, 3, 4, and 5, with darker colours corresponding to lower redshifts. We show in black also the $M_{HI}(M_h)$ obtained considering all galaxies at redshift $z = 0$. At all redshifts, H I is found predominantly in satellite galaxies with halo masses $M_h > 10^{12.5} h^{-1}$ M$_\odot$. For haloes of low and intermediate masses, instead, the dominant contribution comes from central galaxies.

compatible with the values reported in Villaescusa-Navarro et al. (2018). In Fig. 6, we show $M_{HI}(M_h)$ for both the MI and MII simulations, as a function of redshift. We plot the fraction M_{HI}/M_h, to better differentiate results at different redshifts. As discussed in Section 3, we can clearly see the hierarchical growth of structures at the high-mass end, and the AGN feedback inverting the trend at $z = 0$. This is in agreement with the results listed in Table 2: the value of β increases from $z = 5$ to $z = 1$ before dropping at $z = 0$, and the value of M_{break} decreases slowly from $\sim 10^{12} h^{-1}$ M$_\odot$ and rises again at $z = 0$. The presence of the cut-off is more evident at $z = 0$, while a simpler parametrization (without a cut-off) could be adopted at higher redshift. Note that low halo mass end rise of the M_{HI}/M_h fraction for the MI, reflects its poorer resolution that causes a flattening in the M_{HI}–M_h relation near the resolution limit.

To quantify the scatter of the $M_{HI}(M_h)$, we show in Fig. B3 in Appendix B the density distribution of the H I mass hosted by haloes of different mass, at different redshifts.

Equation (2) can be used, as has been done for alternative parametrizations, to create 21 cm mocks from dark matter catalogues. One can use for this a classic HOD approach where each dark matter halo is assigned a total H I content that depends on the halo mass as described by equation (2). One can also add the information about the scatter (Fig. B3). More complex halo occupation models can be constructed by adding additional information that can be extracted from our model.

In Fig. 7, we show the median H I content of dark matter haloes as a function of halo mass for centrals and satellites. At all redshifts, the relation is dominated by central galaxies for small haloes, while for haloes more massive than $M_h \sim 10^{12.5} h^{-1}$ M$_\odot$ the satellites give the dominant contribution. In Appendix B, we propose a parametric model considering separately centrals and satellites. We also give in the appendix the best-fitting values of the parameters for the redshift range $0 < z < 5$, as done in Table 2 for the relation obtained considering all galaxies.

Another interesting property that can be studied with SAMs is the dependence of the H I halo mass function on halo formation time. As a proxy for the halo assembly history, we use the redshift at which a halo has acquired half of its final mass, i.e. z_{50}. We then consider three different samples: (1) young/late assembled haloes as those whose z_{50} falls within the 33th percentile of the distribution; (2) average age haloes as those whose z_{50} is within the 33th and the 66th percentiles; (3) old/early assembly haloes as those whose z_{50} ranges above the 66th percentile. The 33th and 66th percentiles
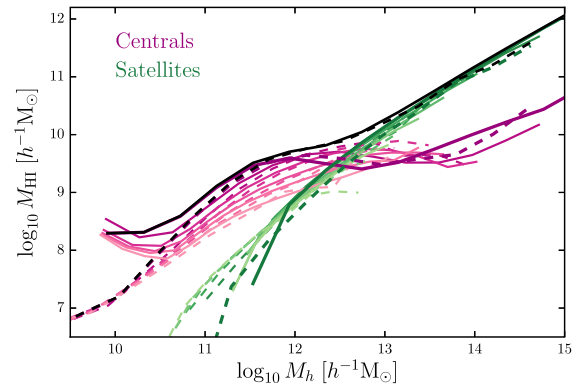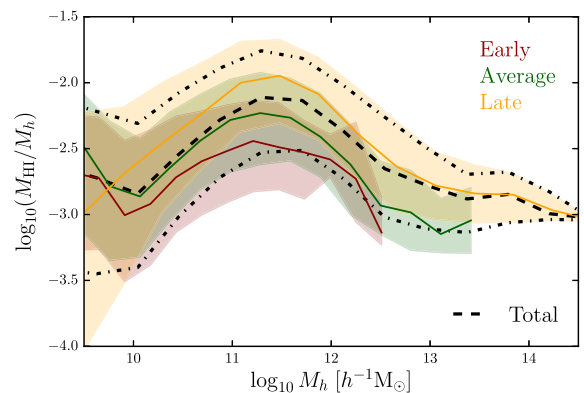

Figure 8. The ratio between the median H I halo mass function $M_{HI}(M_h)$ and M_h for the MII simulation, at redshift $z = 0$ (black dashed), and its 16th and 84th percentiles (black dot–dashed lines). Red, green, and orange lines correspond to the same quantities computed for early, average, and late assembly haloes (see the text for definitions).

are computed on the full z_{50} distribution and correspond to $z = 1.6$ and $z = 2.4$, respectively. In Fig. 8, we show the ratio between the median H I halo mass function and M_h for the MII simulation at redshift $z = 0$, compared to the same relation obtained for haloes with an early, average, and late assembly. In Appendix B, we report the fitting formulas for the relations obtained for the three cases.

The normalization of the relation increases with formation time, explaining in part the scatter of the relation obtained when considering all haloes. For low-mass haloes the total relation coincides with that of haloes with an average assembly history. As halo mass increases the total relation is closer to that obtained for haloes with late assembly times. Comparing Figs 7 and 8, we note that central galaxies dominate the haloes with average formation time at the low-mass end, while at increasing halo mass, the relation is driven by satellites, that are the main contributors to the H I content of late formed haloes. At fixed halo mass, we can interpret the different normalizations of early, average and late formed haloes, as a proxy for the depletion of H I in their satellites. In fact, in our model,
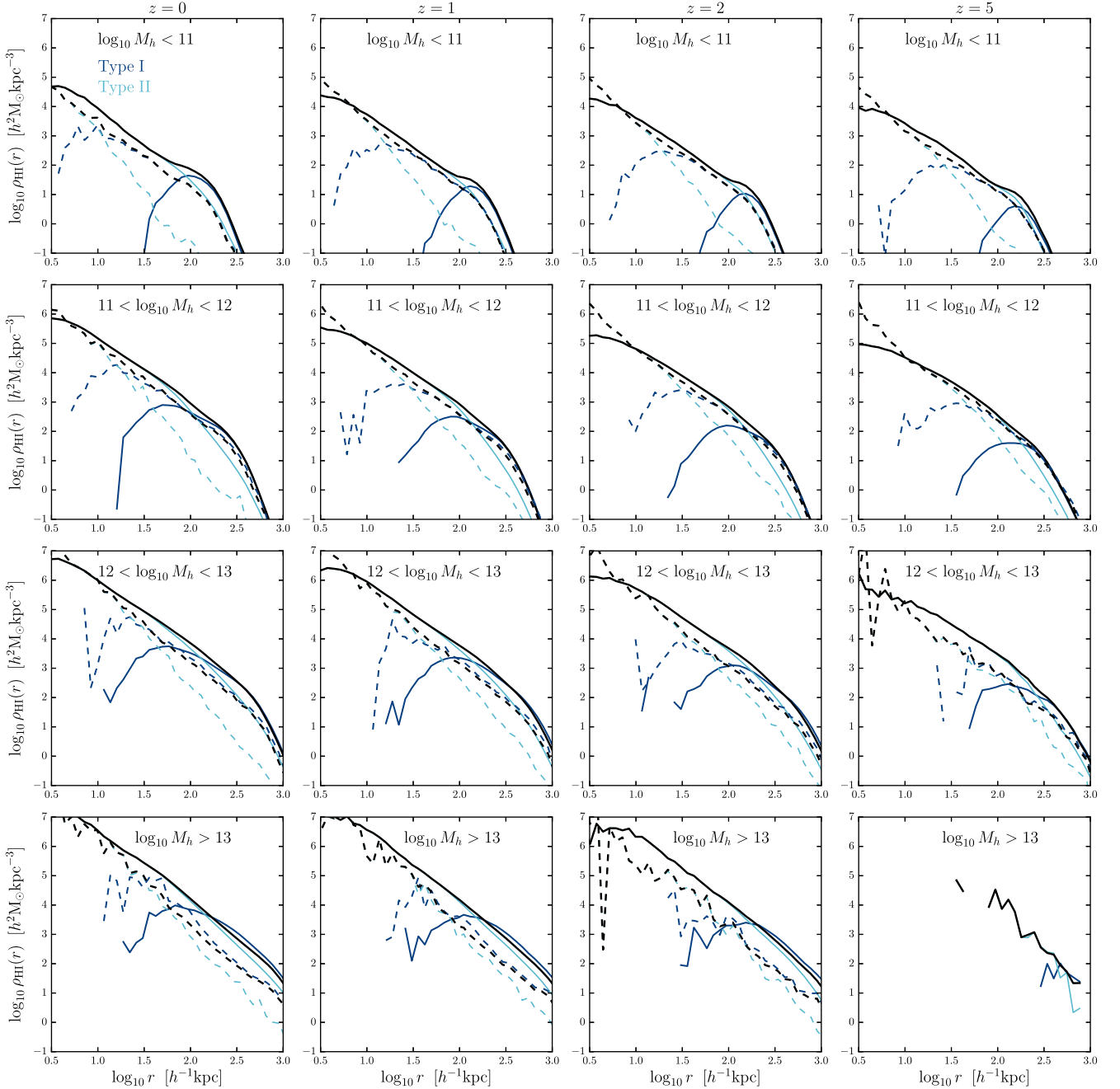
Figure 9. H I profiles of the FoF haloes in the MI (solid lines) and the MII (dashed lines) simulations. FoF haloes are separated in different mass bins ($M_{\rm h}$ is in units of $[h^{-1}\,{\rm M}_\odot]$) at different redshifts, and $\rho_{\rm HI}(r)$ is computed averaging the H I content in spherical shells as a function of the comoving distance from the central galaxy. We also show the H I radial profile obtained considering only Type I (dark blue) and Type II (light blue) satellites. Type I satellites shape the H I profile far from the centre of the haloes, while Type II get much closer. The transition occurs at $r \gtrsim 100 h^{-1}$ kpc for the MI simulation, and at few tens of h^{-1} kpc for the MII.

cooling is possible only on central galaxies, implying that the H I content of satellites can only be depleted. As a result, satellites that reside in same mass haloes that formed later, have had less time to loose H I, dominating the H I content.

5.2 The H I density profile

As seen in Section 5.1, an accurate description of the 21 cm signal down to small scales requires the knowledge of the spatial distribution of H I inside dark matter haloes (the so-called one-

halo term). We compute the H I density profile by summing up the H I mass of satellites in thin spherical shells around the central galaxy of each halo, up to few comoving virial radii. We then divide these profiles according to the total halo mass at different redshifts, and show the average results in Fig. 9. We do not show error bars because the scatter is large and would make the figure too busy. One reason for the large scatter is the non-universality of the H I profiles with respect to dark matter ones (as found also by Villaescusa-Navarro et al. 2018), and the large binning we have used for halo mass. The H I density increases towards the halo centre. This is true

down to the very central regions for the MII, while there is some flattening in the innermost regions ($r < 1\,h^{-1}$ kpc) for the MI, that is likely due to resolution. Indeed, in the MII, the subhaloes are traced down to smaller masses and, consequently, identified down to smaller distances from the halo centre. Generally, we notice that the MII profiles are more concentrated towards the innermost regions of haloes, while the MI profiles tend to be more rounded. Nevertheless, the H I profiles obtained from the MI and MII are roughly in agreement, particularly for haloes of intermediate mass, at all redshifts.

Radial profiles of low-mass haloes are characterized by a knee-like shape far from the centre followed by a pronounced ankle-like feature. This behaviour is less pronounced (in particular for the MI) at higher halo mass. As expected, the profiles are more extended for more massive haloes. We do not find a strong redshift dependence.

As discussed in Section 2, satellite galaxies are divided in two different types: galaxies residing in distinct bound substructures are called Type I, while galaxies whose parent dark matter subhalo has been stripped below the resolution of the simulation are called Type II. Since there is a strong correlation between the time of subhalo accretion and their cluster-centric distance (Gao et al. 2004b), Type II satellites are expected to be more concentrated in the inner regions of dark matter haloes (Gao et al. 2004a). Due to the different resolution limits of the MI and MII, this effect is expected to appear at different radii for these simulations.

To emphasize this behaviour, we consider in Fig. 9 also the contribution from only Type I or Type II satellites. In the outskirts of haloes of all masses, H I is found mainly in Type I satellites. Closer to the centre of haloes, H I is present only in the Type II satellites (the only types of satellites present in the inner regions). The transition occurs at radii $\gtrsim 100\,h^{-1}$ kpc for the MI simulation, and at few tens of h^{-1} kpc for the MII. At the lowest halo masses, the transition is more drastic, making the Type I contribution more visible in the H I profiles.

6 CLUSTERING

The main statistical quantity that can be used as cosmological tool within future 21 cm experiments is the power spectrum of neutral hydrogen. Other statistics can also be used (e.g. Pillepich, Porciani & Matarrese 2007; Breysse, Anderson & Berger 2019; Sarkar, Majumdar & Bharadwaj 2019), and can provide important constraints on e.g. non-Gaussianity (e.g. Cooray 2006; Majumdar et al. 2018).

As discussed when introducing equation (1), several ingredients contribute to the H I power spectrum. In this section, we analyse in detail each of them. In particular, we start giving an estimate of the shot noise in Section 6.1, and we study the bias in Section 6.2.

The first step is the calculation of the H I clustering signal. We use the cloud-in-cell interpolation scheme on a 512^3 grid, and assign to each cell a weight that is equal to the total H I mass hosted by all galaxies in the cell under consideration. We then compute the power spectrum via a fast Fourier transform (FFT) of the values of the density contrast in the grid $\delta_{\rm HI} \equiv \delta\rho_{\rm HI}(\vec{x}, z)/\bar\rho_{\rm HI}(z)$.

$$P_{\rm HI}(k, z) = \left\langle \delta_{\rm HI}\left(\vec{k}, z\right) \delta_{\rm HI}^*\left(\vec{k}, z\right) \right\rangle. \qquad (3)$$

Since the MII has a better mass resolution, the power spectrum can extend to smaller scales than for the MI. On the other hand, the larger volume of the MI (see Table 1) allows larger scales to be sampled.
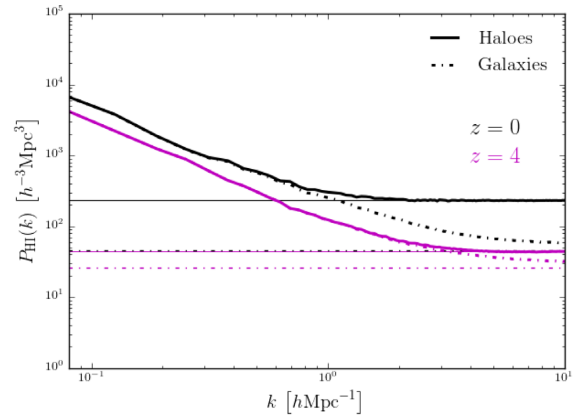

Figure 10. The real space power spectrum of galaxies (dot–dashed lines) for the MII simulation, weighted by their H I mass. Black lines and magenta lines are for $z = 0$ and $z = 4$, respectively. At high k, this can be used to infer the level of shot noise and agrees, as expected, with the estimate that can be obtained using equation 4 (thin dot–dashed lines). We compare it with the 'halo' power spectrum at $z = 0$ (solid black) and $z = 4$ (solid magenta). We define 'halo' power spectrum the one computed considering all the H I content of galaxies at the centre of their hosting halo. The information on the spatial distribution of galaxies inside the halo is thus collapsed on to the central galaxy and the halo power spectrum flattens at larger scales. The shot noise associated with 'haloes' can be estimated from the power spectrum at small scales or using equation (4) (thin solid lines).

Using our SAM, we can analyse in detail the contribution to $P_{\rm HI}(k)$ of sub-samples selected according to different physical properties. Note that we do not re-scale the power spectrum of a sub-sample with respect to the total. If, for example, $\rho_{\rm tot} = \rho_1 + \rho_2$, then P_1 is computed simply as $\langle\delta_1\delta_1^*\rangle$ implying that $P_{\rm tot} \neq P_1 + P_2$. The last equation would translate into an equality only in the case the sub-sample components are added as $P_{\rm tot} = P_1\bar\rho_1/\bar\rho_{\rm tot} + P_2\bar\rho_2/\bar\rho_{\rm tot}$. In the following, we will focus, in particular, on the clustering signal due to haloes of different mass (Section 6.3), on the relative contribution of central and satellite galaxies (Section 6.4), and on the dependence as a function of H I mass (Section 6.5) and colour (Section 6.6). We will see how the results discussed in the previous sections drive the trends that we will discuss in the following. We will often compare $z = 0$ and $z = 4$ to convey a sense of the redshift evolution of some of the properties that we analyse. If not otherwise specified, we use galaxy positions in real space. In Section 6.7, we will relax this assumption and study the clustering in redshift space. This will lead us to the computation of the observable 21 cm power spectrum.

6.1 Shot noise

An important quantity for IM is the shot-noise contribution, which is linked to the discrete nature of the measurement. In Fig. 10, we show the power spectrum $P_{\rm HI}$ for the MII simulation at $z = 0$ and $z = 4$. Since we are dealing with individual galaxies, the shot noise can be measured from the small-scale value of the power spectrum. This value is in agreement with the theoretical expectation, i.e.

$$P_{\rm SN} = \ell_{\rm box}^3 \frac{\sum M_{{\rm HI},i}^2}{(\sum M_{{\rm HI},i})^2}, \qquad (4)$$

where the index i runs over all the H I selected galaxies. The shot-noise values obtained using equation (4) are listed in Table 3. We do not provide the values for the MI simulation since the power spectrum does not flatten significantly at small scales and there is

Table 3. Shot noise $P_{\rm SN}$ [$h^{-3}{\rm Mpc}^3$] as a function of redshift, computed both considering the H I mass in galaxies or collapsing the total H I mass in a halo in the central galaxy. For the MI case, we only list values corresponding to the latter case.

z	0	1	2	3	4	5
MII (gals)	46	61	46	32	26	22
MII (haloes)	232	156	94	61	44	34
MI (haloes)	292	144	114	104	107	134

also the contribution from aliasing; indeed the values obtained with equation (4) are around a factor of two smaller than the small scales value of $P_{\rm HI}$ measured for the MI.

In the halo model, the shot noise is defined as the limit, for $k \rightarrow 0$, of the one-halo term of the H I power spectrum (e.g. Castorina & Villaescusa-Navarro 2017)

$$P_{\rm SN}(z) = \lim_{k \to 0} P_{\rm HI}^{1h}(k, z) = \frac{\int n(M_{\rm h}, z) M_{\rm HI}^2(M_{\rm h}, z) {\rm d}M_{\rm h}}{[\int n(M_{\rm h}, z) M_{\rm HI}(M_{\rm h}, z) {\rm d}M_{\rm h}]^2}. \quad (5)$$

In the limit $k - > 0$ we are looking at the halo as a point-like system. Therefore, the one-halo term flattens to a constant value at large scales and can be considered a shot noise like term. This constant value describes the shot noise in the framework of the halo model since equation (5) has a form similar to equation (4), i.e. the sum of the square of the H I masses divided by the square of the sum of the H I masses. Following Villaescusa-Navarro et al. (2018) and Baugh et al. (2019), we re-compute the H I power spectrum, concentrating all the H I of satellite galaxies in the central galaxy of the corresponding parent halo, thus effectively removing the one-halo contribution. The results, listed in Table 3 and shown in Fig. 10, are in agreement with what expected from equation 4 (in this case, the index i runs over all haloes, and $M_{{\rm HI},i}$ represents the total H I mass in the ith halo). A good agreement is obtained also for the MI, as expected given the fact that we are now considering the shot noise on larger scales.

On large scales, the H I power spectrum obtained for 'galaxies' is identical to that obtained when considering 'haloes', by construction. On smaller scales, where the contribution from satellites is important, the H I power spectrum measured for 'haloes' is flatter than that measured for 'galaxies'. At $z = 0$, this difference is much more pronounced because satellites play an important role. At high redshift, and especially for the MI, the differences become less important. For completeness, we also compute $P_{\rm SN}(z)$ employing equation 5. We use the Sheth and Tormen (Sheth & Tormen 1999) halo mass function for $n(M_{\rm h}, z)$, while for $M_{\rm HI}$ we use the fitting formula given in equation (2) and the values in Table 2. The results obtained are in very good agreement with the ones computed directly from the simulations, demonstrating that of our fitting formula provides a good description of the predicted H I halo mass function. When considering galaxies in the MII simulation, the shot noise increases monotonically going to lower redshift up to $z = 1$, while decreasing at $z = 0$. When considering haloes, it decreases steadily in the MII, while it starts rising again at $z = 3$ for the MI. These complex trends are deeply linked to the evolution of the H I mass function, of the H I density (Section 3), and of the H I halo mass function (Section 5.1). One of the main goal for present and future radio telescopes is the detection of the BAO feature using IM technique. BAOs can be used to constrain the Hubble rate, the angular diameter distance and the growth rate from RSDs (Bull et al. 2015; Bacon et al. 2020). The feasibility of this measurement relies on the strength of the H I power spectrum with respect to the shot-noise level. Following Castorina & Villaescusa-Navarro (2017)
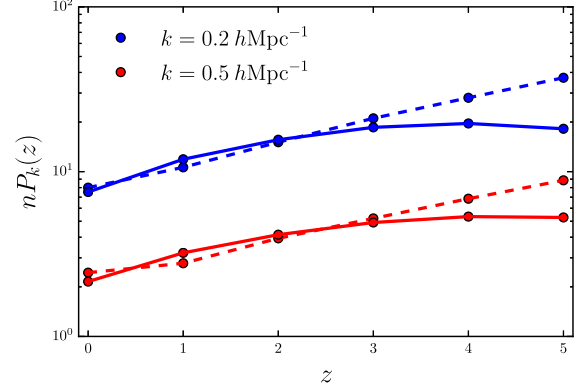
Figure 11. The value of $nP_{0.2}$ (defined in equation 6) as a function of redshift, for the MI (blue solid line) and the MII (blue dashed). As done in Villaescusa-Navarro et al. (2018), we also give the values of $nP_{0.5}$, i.e. $nP_k(z)$ computed at the smaller scale of $k = 0.5 h\,{\rm Mpc}^{-1}$ (red lines). These high values show that shot noise should not be a limitation for 21 cm IM at these scales.

and Villaescusa-Navarro et al. (2018), we compute an approximate quantity that is a proxy for the signal to noise:

$$nP_{0.2}(z) = P_{\rm HI}(k = 0.2 \, h{\rm Mpc}^{-1}, z)/P_{\rm SN}(z). \quad (6)$$

We show how this quantity evolves as a function of redshift in Fig. 11, for both the MI and the MII. The values are consistent, although slightly lower than those reported in Villaescusa-Navarro et al. (2018), showing that the shot-noise contamination should not be a problem at the BAO scale. The same quantity computed at $k = 0.5 \, h\,{\rm Mpc}^{-1}$ shows that also smaller scales should be available for 21 cm IM.

6.2 H I bias

Although an IM H I survey will collect information on the neutral hydrogen content of the Universe, the information about the cosmological parameters is ultimately carried by the dark matter distribution. To understand the relation between the H I clustering and the underlying dark matter distribution, it is thus crucial to study the amplitude and shape of the H I bias, $b_{\rm HI}$, defined in equation 1. One can write

$$b_{\rm HI}(k) = \sqrt{(P_{\rm HI}(k) - P_{\rm SN})/P_{\rm m}(k)}, \quad (7)$$

where $P_{\rm SN}$ is the shot-noise contribution described in Section 6.1. The bias can be measured on simulations simply computing the H I power spectrum (shot noise subtracted) and the matter power spectrum $P_{\rm m}(k)$. On large scales, $b_{\rm HI}(k)$ is expected to be roughly constant, while at small scales it has a more complex behaviour (e.g. Guha Sarkar et al. 2012; Camera et al. 2013; Pénin, Umeh & Santos 2018). This is shown in Fig. 12, where the large-scale measurements are noisy due to sample variance. Indeed, if we compute the bias using the theoretical $P_{\rm m}(k)$ instead of that measured directly from simulations,[1] the large-scale value of the bias becomes constant and agrees quite well between the MI and MII simulation. We list the value of the bias as a function of redshift in Table 4. Our results are in quite good agreement with those found in Villaescusa-Navarro et al. (2018). Similarly to what found in other studies (e.g. Marín

---

[1]For the MII, measured $P_{\rm m}(k)$ are publicly available only for some of the redshifts used in this study.
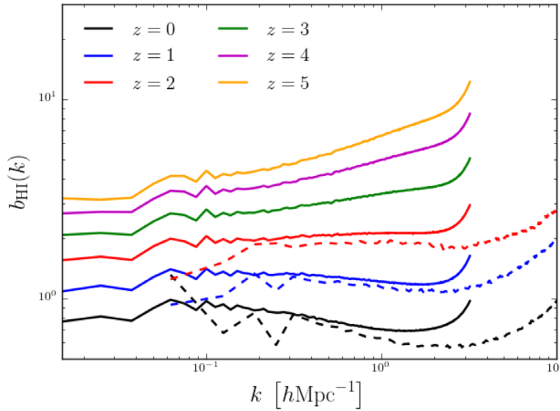
Figure 12. The H I bias defined as the square root of the ratio between the H I power spectrum and the dark matter power spectrum, for the MI (solid lines) and the MII (dashed lines), at different redshifts (different colours).

Table 4. The approximate value of the H I bias b_{HI} at large scales, computed as in equation (7) using the linear theory prediction for the matter power spectrum. These results are obtained averaging the values of $b_{HI}(k)$ in first few k-bins, going from $k = 0.01$ up to $0.02\,h\,\mathrm{Mpc}^{-1}$ for the MI, and from $k = 0.06$ to $0.13\,h\,\mathrm{Mpc}^{-1}$ for the MII. In these ranges of scales, the bias is about constant. Moreover, there is good agreement between the MI and the MII.

z	0	1	2	3	4	5
MI	0.87	1.22	1.76	2.36	2.98	3.73
MII	0.89	1.31	1.74	2.18	2.65	3.18

et al. 2010; Villaescusa-Navarro et al. 2018; Ando et al. 2019; Baugh et al. 2019), the bias grows with redshift, showing that H I is more clustered than dark matter, and its $z = 0$ value at large scales is roughly in agreement with the standard value of 0.85 (e.g. Marín et al. 2010). The significant increase of b_{HI} with redshift is important for IM experiments, since it will make the 21 cm signal stronger. At $z = 0$, the bias predicted from our model shows a scale dependence starting from $k \sim 0.1\,h\,\mathrm{Mpc}^{-1}$, with a dip around $k \sim 1\,h\,\mathrm{Mpc}^{-1}$. This has been found also in preliminary observational measurements (Anderson et al. 2018), and in independent studies based on hydrodynamical simulations (Villaescusa-Navarro et al. 2018). We will discuss this further in Section 6.6. The position of the minimum changes slightly between the MI and the MII, indicating a possible effect of resolution. Note, however, that this can be partially justified by imperfect shot-noise subtraction in the MI, causing an upturn at larger scales. Up to $z = 2$, the bias is roughly constant down to $k \sim 2\,h\,\mathrm{Mpc}^{-1}$, while at higher redshift the scale dependence is already noticeable at $k \sim 0.3\,h\,\mathrm{Mpc}^{-1}$.

6.3 Clustering and halo mass

In this section, we analyse the H I mass weighted galaxy power spectrum $P_{HI}(k)$, focusing on its dependence on the halo mass. These results can be understood from the conditional H I mass function (Section 3.1) and the H I halo mass function (Section 5.1).

In Fig. 13, we show the H I power spectrum $P_{HI}(k)$ at $z = 0$ (top) and $z = 4$ (bottom panel), computed by considering H I in galaxies hosted by haloes of increasing minimum mass. These power spectra are compared to the total neutral hydrogen power spectrum that is calculated using all the galaxies in the simulations (selected using the stellar mass cuts presented in Table 1). At $z = 0$, the total neutral
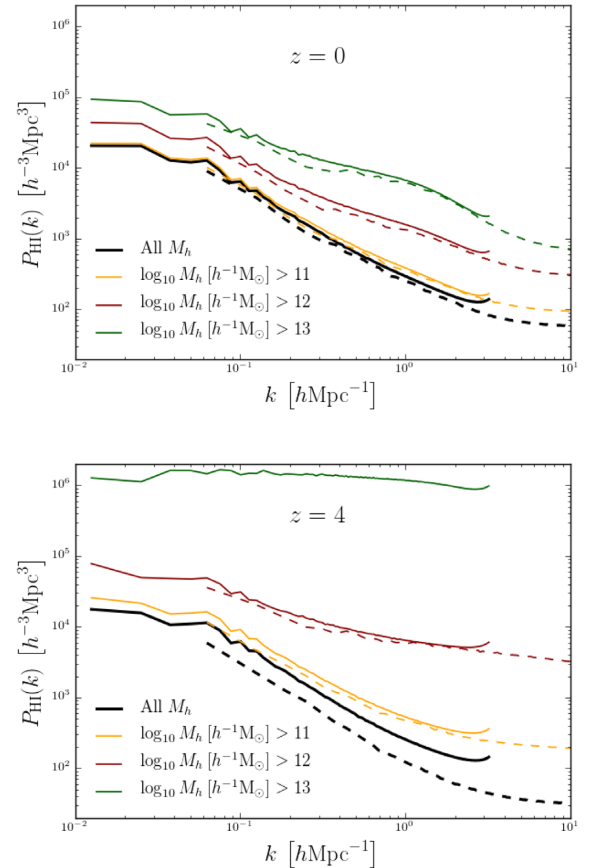

Figure 13. *Top panel*: The H I power spectrum considering all galaxies (black lines) in the MI (solid) and MII (dashed lines) simulations, at $z = 0$. We further consider the contribution due to haloes of increasing mass (different colours, as in the legend). *Bottom panel*: Same as for the top panel, but at $z = 4$.

hydrogen power spectra of the MI and MII are in good agreement for all the scales that they have in common, indicating that they are describing similar H I distributions.[2] Rising the halo mass threshold, the amplitude of the power spectrum increases revealing the halo bias, namely more massive haloes are expected to be more clustered. Excluding low-mass haloes ($M_h > 10^{11}\,h^{-1}\,\mathrm{M_\odot}$), the clustering increases only on small scales, indicating that the large-scale structure is not driven by these small haloes in either the MI and MII simulation. As discussed in Section 5.1, most of the H I in the most massive haloes ($M_h > 10^{13}\,h^{-1}\,\mathrm{M_\odot}$) is hosted in an increasing number of H I-poor satellite galaxies, i.e. this is sampling the one-halo term. We will discuss the role of satellites further in Section 6.4.

At higher redshift ($z = 4$ in the bottom panel of Fig. 13), the $P_{HI}(k)$ evaluated considering all haloes from the MI and MII do not agree. The reason for this can be found in the different H I mass functions for the MI and the MII (see Fig. 3). At $z = 0$, most of the galaxies of both simulations have H I masses in the convergent part of the H I mass functions. At high redshift, high H I mass galaxies are not yet formed, resulting in suppressed tails of the H I mass functions. This enhances the relative importance of the low-mass

---

[2]The deviation between the MI and the MII around $k \sim 3h\,\mathrm{Mpc}^{-1}$ is due to residual aliasing from unresolved small-scale modes due to the finite FFT grid (Sefusatti et al. 2016), and should not be considered in the discussion.
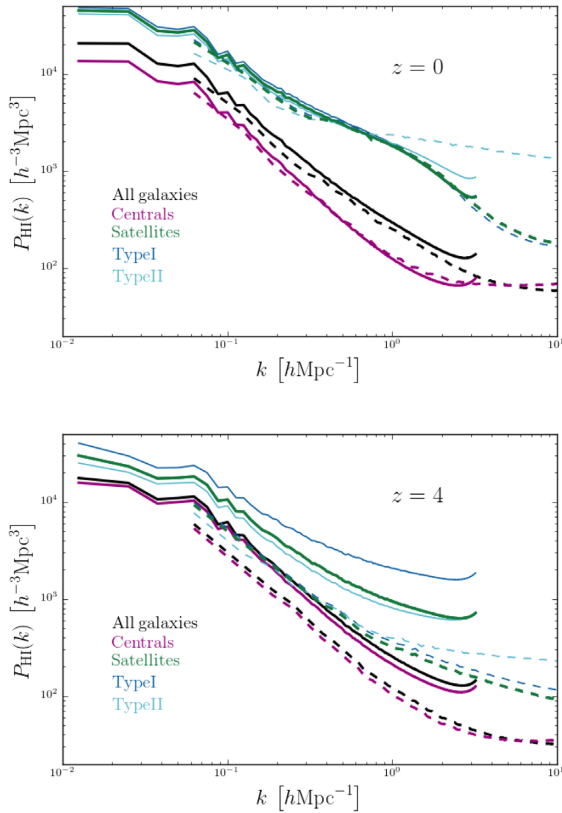
Figure 14. *Top panel*: The power spectrum of H I selected galaxies at $z = 0$ in the MI (solid) and MII (dashed lines) simulations, considering separately the contribution from centrals (magenta) and satellites (green). Satellite galaxies are further divided into Type I (dark blue) and Type II (light blue). The total H I power spectrum (black) is the same as the one in Fig. 13. *Bottom panel*: Same as in the top panel, but at $z = 4$.

end, where MI and MII diverge. This is in agreement with what expected from Fig. 3: the convergence limit between the MI and MII is higher at higher redshift.

Rising the minimum halo mass above $10^{11} \, h^{-1} \, \mathrm{M_\odot}$ will select indirectly galaxies with H I masses mostly $\gtrsim 10^8 \, h^{-1} \, \mathrm{M_\odot}$ (see Fig. B3), avoiding the divergent part. As a consequence, the halo mass selection erases the differences between MI and MII power spectra. The normalization increases again with halo mass threshold, as a result of halo bias. Note that there are only very few very massive haloes ($M_h > 10^{13} \, h^{-1} \, \mathrm{M_\odot}$) in MI at this redshift, and none in the volume of MII. For this reason, we can see only a highly biased shot noise in the case of MI.

6.4 Clustering of central and satellite galaxies

To build a clearer picture of the role of satellite and central galaxies in the distribution of neutral hydrogen, we show in Fig. 14 the H I power spectra computed considering these different types of galaxies, at $z = 0$ and $z = 4$ (top and bottom panels). The black lines in this figure represent the total H I power spectrum, as in Fig. 13. The H I power spectra of satellite and central galaxies have, respectively, higher and lower amplitude than the total H I power spectrum, for both MI and MII, at all redshifts. As discussed in Section 5.1, the neutral hydrogen is hosted mainly by central galaxies in small haloes, while large amounts of H I is hosted by satellite galaxies in the most massive haloes (see Fig. 7). This

implies that the $P_{\mathrm{HI}}(k)$ of satellites should be higher than that of centrals, because it is due a population with larger bias. The difference is more pronounced at $z = 0$ than at $z = 4$, because of the larger number densities of massive haloes. At $z = 0$, we also expect the power spectrum of satellites to be similar to that obtained when considering only massive haloes (top panel of Fig. 13): this is indeed the case, and we recognize the shape of the one-halo term.

At $z = 4$, in the MII, satellites and massive haloes are far less numerous than in the MI. As a consequence, there is no strong correlation between satellites and massive haloes in the MII, namely a selection based on galaxy type does not necessarily translate into a selection in halo mass. Indeed, in the bottom panel of Fig. 14, we see a clear deviation between the H I power spectra of the satellites in MI and MII. This behaviour is found also when comparing the H I mass functions of satellites in the MI and MII at $z = 4$, as shown in Fig. A1. In the same figure, the differences between the H I mass functions of central galaxies in MI and MII can justify the different power spectra we obtain at $z = 4$ in Fig. 14, since the bulk of the centrals population in MII is peaked around a lower M_{HI} with respect to MI.

We then compute the $P_{\mathrm{HI}}(k)$ considering separately Type I and Type II satellites. Type I are accreted more recently and are more numerous than Type II, especially at high redshift. As can be seen also in Fig. 9, Type I satellites hosting H I are more common in massive haloes. Since dark matter halo bias is stronger for more massive haloes, the neutral hydrogen power spectrum of Type I satellites is larger than that of Type II, at all redshifts and for both MI and MII, for $k < 0.6 \, h \, \mathrm{Mpc}^{-1}$. In Section 5.2, we have seen that the inner part of H I profiles is dominated by Type II satellites that have had the time to drift to the inner regions of haloes, in particular for the MII. In terms of small-scale power spectrum, this effect translates into a relatively high shot-noise term, since we are effectively almost tracing the power spectrum of massive haloes.

6.5 Clustering as a function of H I mass

In this section, we study how the H I power spectrum depends on the H I threshold adopted, similarly to what has been done in e.g. Kim et al. (2015, see also Zoldan et al. 2017). We show in Fig. 15 the H I power spectra calculated selecting galaxies using three different H I mass thresholds and compare them to the total H I power spectrum (in black, as in Fig. 13).

At $z = 0$, for both the MI and MII, the $P_{\mathrm{HI}}(k)$, for $k \lesssim 1 \, h \, \mathrm{Mpc}^{-1}$, does not depend significantly on the H I mass threshold adopted. Indeed, as discussed in Section 5, galaxies of different H I mass are distributed evenly across haloes of different mass (see Fig. 2). Only the highest threshold ($M_{\mathrm{HI}} > 10^9 \, h^{-1} \, \mathrm{M_\odot}$) leads to a rise of the shot noise in the MII simulation on small scales. This happens because this cut removes completely the lowest mass haloes.

At $z = 4$, we get higher amplitudes of the H I power spectra for higher H I mass thresholds, in particular for $M_{\mathrm{HI}} \gtrsim 10^8 \, h^{-1} \, \mathrm{M_\odot}$. These moderately H I-rich galaxies populate mainly massive haloes at this redshift, and their power spectra reflect the halo bias. This is valid for both MI and MII, and increasing the H I mass threshold, the amplitudes of the MI and MII power spectra get into good agreement, because the threshold progressively matches the convergence mass between the two simulations.

In Fig. 16, we analyse the same relations but this time considering only satellite galaxies at $z = 0$. We show as a comparison the satellite total H I power spectrum (the green line as in top panel of Fig. 14). Removing the low H I mass population partially erases the one-halo term in the MII and completely in the MI, erasing
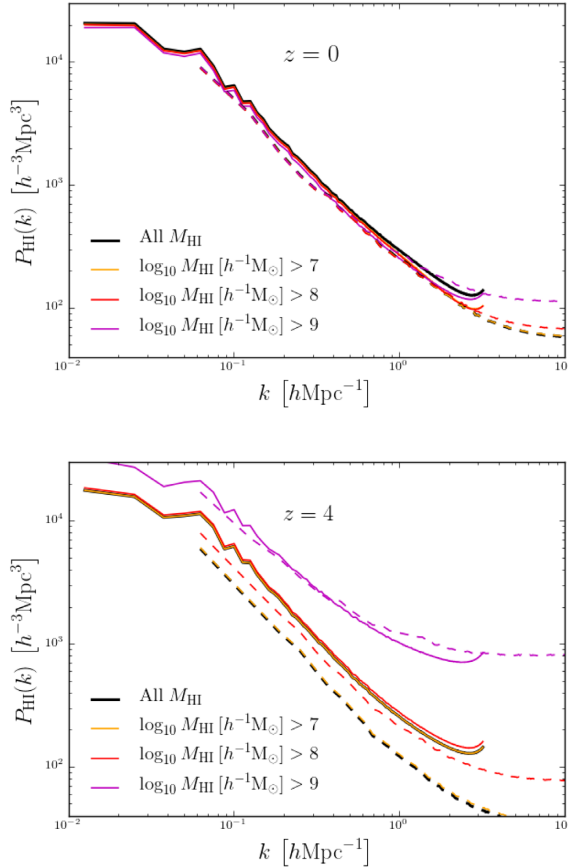
Figure 15. *Top panel*: The power spectrum of H I selected galaxies at $z = 0$ in the MI (solid) and MII (dashed lines) simulations, computed selecting galaxies with progressively larger H I mass. The total H I power spectrum (black) is the same as the one in Fig. 13. *Bottom panel*: Same as in the top panel, but at $z = 4$.
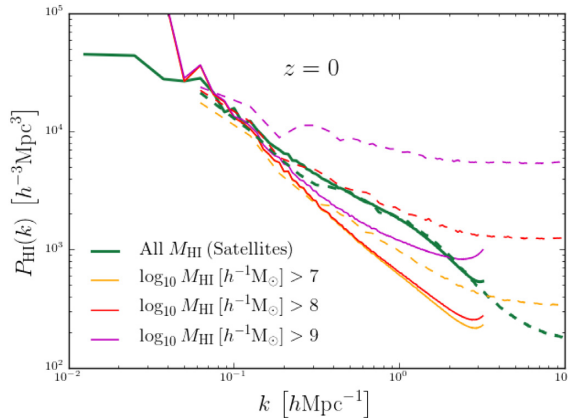

Figure 16. The power spectrum of H I selected satellite galaxies at $z = 0$ in the MI (solid) and MII (dashed lines) simulations, computed selecting satellites with progressively larger H I mass. The total satellite H I power spectrum is the same as the green one in Fig. 14.

also the agreement between the two simulations. The H I poor galaxies represent an important contribution to the one-halo term. This is true for both simulations even if the number of low-mass H I galaxies is higher in the MII, due to its better mass resolution. Increasing the H I mass threshold does not affect significantly $P_{\rm HI}(k)$

at intermediate scales, since satellites are distributed in haloes of all masses (see Fig. 2). The increasing threshold has, however, an important effect on smaller scales: removing an increasing number of galaxies rises the shot-noise contribution. This effect is stronger for the MII because satellites are less numerous than in the MI for $M_{\rm HI} \gtrsim 10^8 \, h^{-1} \, {\rm M_\odot}$ (see Fig. 1).

6.6 Red and blue galaxies

As seen in Section 6.2, the $z = 0$ bias has a spoon shape scale dependence that seems to be present in observational data (see Fig. 12). Indeed, Anderson et al. (2018) have found a statistically significant decrement of the 21 cm intensity × galaxy cross-power spectrum at $k \sim 1.5 \, h \, {\rm Mpc^{-1}}$, at $z \sim 0.08$. They ascribe this behaviour to a combination of lack of H I clustering and lack of correlation between H I and optical galaxies. In particular, they find a scale and colour-dependent correlation coefficient between H I and galaxies. The spoon shape present in our results is indeed a sign of lack of H I clustering at those scales. In this section, we investigate further the decrease of the H I bias at $k \sim 1 - 2 \, h \, {\rm Mpc^{-1}}$, and how it relates to the red or the blue galaxy population.

We focus our analysis at $z = 0$, and select red and blue galaxies using a cut in specific star formation rate, i.e. defining a galaxy as blue if sSFR $> 0.3/t_{\rm H} \, [{\rm Gyr^{-1}}]$, where $t_{\rm H}$ is the Hubble time (see e.g. Gonzalez-Perez et al. 2017). In our model, the fraction of red passive galaxies is around 20 per cent for $M_{\rm s} < 10^{10.5} \, h^{-1} \, {\rm M_\odot}$, while steadily rising to more than 80 per cent for the most massive galaxies. Despite the presence of massive passive galaxies, red galaxies overall represent less than the 20 per cent of our sample at $z = 0$. The majority of these red galaxies have low H I masses ($M_{\rm HI} < 10^8 \, h^{-1} \, {\rm M_\odot}$). In the top panel of Fig. 17, we show the H I halo mass function for red and blue galaxies. The red population is mostly found in massive haloes with high halo bias, as most satellites in these massive haloes are red galaxies. This can be seen in the bottom panel of Fig. 17, where we show the H I power spectra for the selected red and blue galaxies. The H I power spectrum of red galaxies has a larger amplitude than found for the total and blue H I power spectra. For the MI, the presence of a visible one-halo term indicates a large population of old H I poor red galaxies that populate the inner regions of massive haloes. The blue star-forming population dominates the H I content of medium mass haloes, and follows very well the clustering obtained when considering the total H I power spectrum. The $P_{\rm HI}(k)$ is, in this case, lower than the total one at all scales because the red population gives an important contribution in the very massive haloes. In addition, the blue population is less clustered than the overall population in the MI at small scales, while in the MII there is a rise of the shot noise.

For completeness, we compute, using equation (7), the bias for the H I rich blue galaxies and H I poor red galaxies. The results are shown in Fig. 18. We see that the lack of clustering at small scales for the blue population results in an enhanced spoon shape at $k \sim 1-2 \, h \, {\rm Mpc^{-1}}$. This is in agreement with what found by Anderson et al. (2018), i.e. H I is strongly correlated to blue star-forming galaxies. We see a different behaviour for the red population, especially at the scales sampling the one-halo term and the shot noise. This difference is more pronounced for the MI simulation. The reason for a stronger bias of the red population in the MI with respect to the MII simulation can be found in the way the fraction of passive galaxies rises with halo mass: in the MII, a large fraction of galaxies in haloes of $\sim 10^{12} \, h^{-1} \, {\rm M_\odot}$ are passive, while in the MI the same passive fraction is reached at larger halo masses

Figure 18. The total H I bias b_{HI} (see equation 7) compared to the one computed selecting the blue and red population, for both the MI (solid lines) and the MII (dashed lines). A galaxy is defined blue if its specific star formation rate is larger than sSFR $> 0.3/t_H$ [Gyr^{-1}], where t_H is the Hubble time.
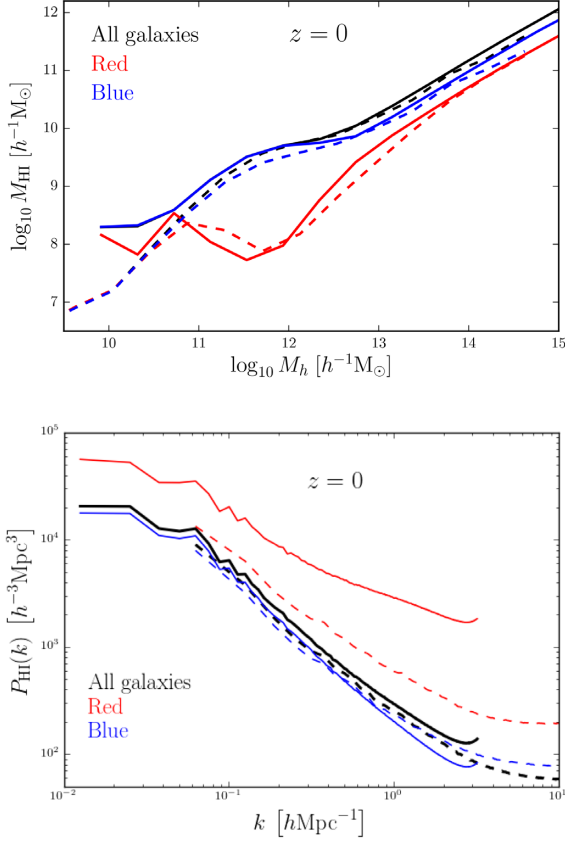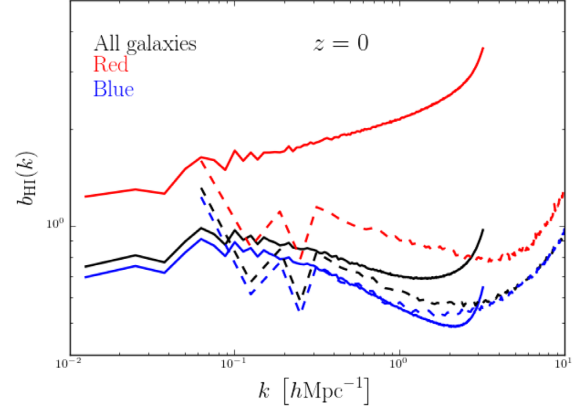
Figure 17. *Top panel*: The H I content of dark matter haloes as a function of halo mass, separating the contribution from red and blue galaxies (lines of corresponding colours). We consider as blue galaxies those with sSFR $> 0.3/t_H$ [Gyr^{-1}]. Blue galaxies dominate the H I content of intermediate mass haloes, while red galaxies are mostly found in very massive haloes. *Bottom panel*: The power spectrum of the red and blue populations (colour coded accordingly) compared to the total one for the MI (solid lines) and the MII (dashed lines).

($\sim 10^{13} \, h^{-1} \, M_\odot$). The net effect is that, for the MI, we are looking at a population with stronger halo bias.

6.7 H I signal in redshift space

It is well known that peculiar velocities of galaxies cause a Doppler shift that distorts the shape of the observed power spectrum, enhancing the clustering on large scales (Kaiser 1987), and suppressing it on the smaller scales (the Finger-of-God effect). In this section, we compute the H I power spectrum in redshift space $P_{HI}^{RS}(k)$, using the plane-parallel approximation to displace the galaxy positions:

$$s = r + \frac{1+z}{H(z)}(v(r) \cdot \hat{z})\hat{z}. \tag{8}$$

In the above equation, r is the galaxy position in real space, $v(r)$ is its peculiar velocity, and we assume that the z-axis is the line of sight. The results are shown in the top sub-panels of Fig. 19, for $z = 0$ (top) and $z = 4$ (bottom panels). As done already by other authors, it is interesting to compute the linear theory prediction for the Kaiser effect:

$$\frac{P_{HI}^{RS}}{P_{HI}} \sim 1 + \frac{2}{3}\beta + \frac{1}{5}\beta^2 \tag{9}$$

to test its validity against the simulation results. In the above equation, $\beta = f/b_{HI}$, with $f \simeq \Omega_m^{0.545}(z)$ the linear growth rate. For the bias b_{HI}, we have used the approximate results of Table 4. Being the estimation of the bias slightly different for the MI and MII, we show two different limits in the lower sub-panels of Fig. 19. These should be compared with the results from simulations: as expected, the minimum scale at which the Kaiser limit is valid increases at higher redshift. At $z = 4$, linear theory works nicely down to $k \sim 0.5 \, h \, \text{Mpc}^{-1}$.

From the power spectrum in redshift space measured in our simulations, we can extract a prediction for the 21 cm signal for future IM experiments. We rewrite the 21 cm power spectrum of equation (1) as (Wyithe & Brown 2010):

$$P_{21\,cm}(k) = T_b^2 P_{HI}^{RS}(k) \tag{10}$$

and use (Furlanetto et al. 2006)

$$T_b = 23.88 x_{HI} \left(\frac{\Omega_b \, h^2}{0.02}\right) \sqrt{\frac{0.15}{\Omega_m \, h^2} \frac{(1+z)}{10}} \, \text{mK}. \tag{11}$$

T_b depends on the brightness temperature contrast on the fraction of neutral atomic hydrogen $x_{HI} \equiv \Omega_{HI}/\Omega_H$. We estimate the hydrogen fraction as $\Omega_H = 0.74\Omega_b$. The results are shown in the top panel of Fig. 20, for both the MI and the MII and for different redshifts. The $P_{21cm}(k)$ decreases with redshift as does Ω_{HI} (Fig. 4). For completeness, we show in the bottom panel of Fig. 20 the quantity $\Delta_{21\,cm}(k) \equiv P_{21\,cm}(k)k^3/2\pi^2$. Our assumed value for Ω_{HI} affects the amplitude of $P_{21cm}(k)$ that is proportional to $(\Omega_{HI}b_{HI})^2$ at large scales. This affects our predictions especially at high redshift, where our SAM is offset low with respect to observational measurements (see Section 4). The decrease of Ω_{HI} is partially compensated by the increase of the bias b_{HI} (see Section 6.2). The slightly larger value of Ω_{HI} at $z \gtrsim 3$ found for the MII simulation with respect to the MI, raises the absolute scale of the MII $P_{21cm}(k)$ with respect to the one of the MI simulation, inverting the trend discussed for the $P_{HI}(k)$ at high redshift (see lower panel of Figs 13 and 19).

7 CONCLUSIONS

The upcoming new era of neutral hydrogen (H I) experiments bears the potential to significantly advance our knowledge of

the Universe. 21 cm IM surveys are being planned, to map H I within unprecedented volumes of the Universe, integrating the signal from hundreds of galaxies in large tri-dimensional pixels. A realistic modelling of the expected H I signal cannot refrain from understanding the role of H I in galaxy evolution. Moreover, to fully exploit forthcoming data for cosmological experiments, it is fundamental to elucidate how H I relates to the underlying dark matter distribution. To this aim, SAMs represent a privileged and flexible tool to understand the main physical processes that regulate H I in galaxies, starting from a cosmological dark matter distribution.

In this paper, we have used the GAEA model for studying neutral hydrogen in the post-reionization Universe. This state-of-the-art SAM comprises, among other physical prescriptions typically included, metal and energy recycling with a non-instantaneous approximation, an explicit treatment for the cold gas partition into atomic (H I) and molecular (H$_2$) hydrogen, and a star formation law based on the surface density of molecular hydrogen. GAEA has been run on merger trees extracted from the Millennium I (MI) and the Millennium II (MII) *N*-body simulations. The latter samples a smaller volume but has a factor ten better resolution than the former. We have taken advantage of this duality to analyse the distribution of H I in galaxies, as a function of halo mass and cosmic epoch.

7.1 Modelling the H I distribution in dark matter haloes

In the first part of our work, we have analysed in detail predictions from the GAEA model with the goal to understand optimal methods to model the H I distribution. Given the large volumes involved, and the difficulties to model the formation and evolution of atomic hydrogen from first principles, most of the research in the field relies on statistical methods to populate dark matter haloes with H I (e.g. HOD approaches). In fact, these represent the only possible tools to construct large numbers of 21 cm maps covering large cosmological volumes, without prohibitive computational costs. The approach also allows the exploration of different physical models for the H I evolution, as well as of different cosmological models. Our simulations are well suited for this task because they reproduce well the H I distribution measured in the local Universe. We have used our simulated catalogues to characterize in detail the H I distribution and explain the origin of the relation between H I mass and halo mass in our model. We summarize here our results.

(i) The galaxy H I mass function (HIMF) is dominated by central galaxies at intermediate and large H I masses, while satellite galaxies become increasingly important at low masses. The total HIMF results in a complex convolution of galaxies residing in haloes with a broad range of masses. At low H I masses, the main contributions come from satellites in haloes of all masses, while at larger H I masses the main contribution comes from central galaxies of increasing halo mass. These general trends are shared by independent SAMs (e.g. Lagos et al. 2011; Kim et al. 2017) and therefore do not depend on the particular physical prescriptions adopted.

(ii) The number density of galaxies with low H I masses does not evolve significantly with cosmic time, up to $z \sim 5$. The mild dependence on redshift can be ascribed to the growing number of satellites towards later epochs. At large H I masses, the evolution as a function of redshift is much stronger and traces the hierarchical formation of progressively more massive haloes. Independent published theoretical models provide different predictions for the evolution of the HIMF with typically a stronger evolution of the number density
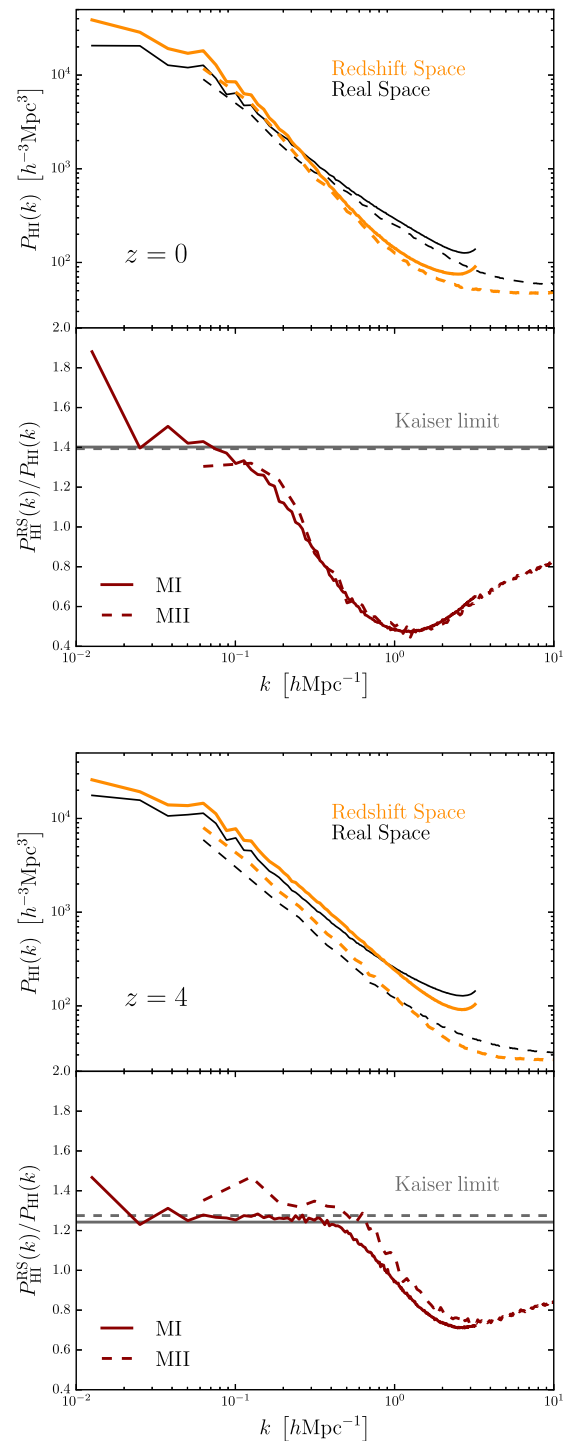

Figure 19. Comparison between the H I power spectrum computed in real space (black) and in redshift space (orange), for the MI (solid) and MII simulations (dashed lines), for $z = 0$ (top) and $z = 4$ (bottom panels). In the lower sub-panel of each panel, we show the Kaiser limit for both the MI (grey solid) and the MII (grey dashed), computed as in equation (9), and compared to what is measured in simulations.

at low H I masses (Lagos et al. 2011; Davé et al. 2017; Baugh et al. 2019). Observational measurements are still lacking beyond the local Universe, therefore future data will provide important constraints on our galaxy formation models for example confirming
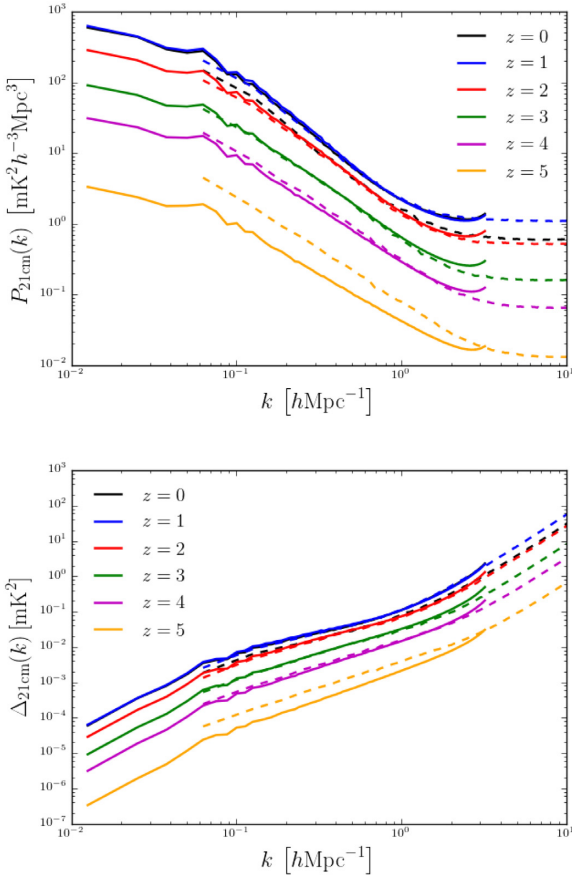
Figure 20. The power spectrum of the 21 cm signal $P_{21\,\mathrm{cm}}(k)$ (top panel) and the $\Delta_{21\,\mathrm{cm}}(k) \equiv P_{21\,\mathrm{cm}}(k)k^3/2\pi^2$ (bottom panel) as predicted from the MI (solid lines) and the MII (dashed lines), at different redshifts (from $z = 0$ to 5, colour coded as in legend).

or refuting the importance of satellite galaxies for the evolution of gas at high redshift.

(iii) Our model predicts a mild decline of the cosmic density of atomic hydrogen $\rho_{H_I}(z)$. This is in tension with observational data based on DLAs. A better and complete understanding of this disagreement is beyond the scopes of this work. We have demonstrated that this can be only in small part explained by the limited resolution of our simulations, and the expected increasing contribution from low-mass haloes at increasing cosmic epochs. In fact, very small haloes do not host significant amounts of H_I because of cosmic reionization (see also Villaescusa-Navarro et al. 2018). The decreasing cosmic density of H_I in our model should be probably ascribed to the presence of H_I outside haloes that, based on hydrodynamical simulations, can contribute to up to ~ 20 per cent of the total H_I at high redshift (Villaescusa-Navarro et al. 2014; Diemer et al. 2018; Villaescusa-Navarro et al. 2018). It is worth noting, however, that some of the simulations that exhibit a flatter, or even rising trend for the cosmic density of H_I, are those that predict an increasing peak in the low-mass end of the HIMF (see e.g. figs 7 and 12 in Popping et al. 2014, fig. 4 in Baugh et al. 2019, or figs 7 and 9 in Davé et al. 2017).

The analysis of the HIMF lays the foundation to characterize the halo H_I mass function $M_{H_I}(M_h)$, i.e. the total H_I content of dark matter haloes as a function of halo mass. This is a key element in the construction of IM mock maps with HOD techniques, and several

empirical relations can be found in the literature, ranging from simple power-law behaviours to more complex parametrizations (e.g. Bagla et al. 2010; Barnes & Haehnelt 2010; Santos et al. 2015; Villaescusa-Navarro et al. 2018; Baugh et al. 2019; Obuljen et al. 2019). We have proposed a fitting formula based on our simulated data that is characterized by (i) a correction to the standard power-law behaviour at large halo mass, that is due to the effect of AGN feedback (as already proposed by Baugh et al. 2019) and (ii) a low-mass cut-off, expected from cosmic reionization. Our best-fitting parameters are listed in Table 2, and are given from redshift $z = 0$ up to $z = 5$. To better characterize the relation between H_I and halo masses, we have analysed how the scatter of the halo H_I mass function depends on the formation history of haloes, using as a proxy the time when half of the mass was assembled. We find that the halo formation time is the main driver of the scatter of the halo H_I mass function, with its normalization increasing with increasing formation time. HOD models typically do not account for this dependence on assembly bias, that is however important for cosmology precision. We have provided fitting functions for both central and satellite galaxies, and different assembly histories (Tables B1–B3). These relations can be applied to construct refined HOD models that can be used to generate 21 cm mock maps. We intend to pursue this goal in future work.

7.2 Estimates for future intensity mapping experiments

One of the main tools that will be used to analyse future IM experiments is the power spectrum of the neutral hydrogen distribution. In the second part of our work, we have analysed the shape of the H_I mass weighted power spectrum $P_{H_I}(k)$, as predicted by GAEA. Thanks to the flexibility of our SAM, the total H_I distribution can be dissected as a function of different galaxy properties, quantifying the contribution from shot noise and galaxy bias. Our main results are summarized in what follows.

(i) Our model predicts a flattening of the power spectrum at small scales, in quantitative agreement with the expected value of the H_I mass weighted galaxy shot noise (see equation 4). We have also computed the shot-noise level as proposed in Villaescusa-Navarro et al. (2018), concentrating all H_I inside dark matter haloes at their centre, consistently with the shot-noise definition of the halo model (see equation 5). We predict a steadily decrease of the shot noise with redshift in this case. Our results confirms that shot noise will not limit the capability of measuring the BAO features with IM experiments.

(ii) We find that the H_I bias, b_{H_I}, increases with redshift, and shows a characteristic dip at $k \sim 1h\,\mathrm{Mpc}^{-1}$ in the local Universe, in qualitative agreement with observational measurements of Anderson et al. (2018). This 'feature', due to lack of H_I clustering at those scales, has been investigated further by considering the different contribution from blue/active and red/passive galaxies. The former dominate the total H_I content of dark matter haloes, especially at intermediate halo mass, providing a more accurate description of the H_I clustering; the latter, in contrast, dominate the central regions of the most massive haloes.

(iii) The amplitude of the power spectrum increases when selecting galaxies residing in progressively more massive haloes. At $z = 0$ and for massive haloes, an increasing number of satellites reveals the one-halo term contribution in the power spectrum. At $z = 4$, these massive haloes are not yet assembled, and the resulting power spectrum reflects a highly biased shot-noise term. At low redshift, the H_I power spectrum does not depend significantly on

the H I threshold adopted, because H I galaxies of given mass are distributed across a wide range of halo masses. At all scales, an important contribution to the H I power spectrum is provided by satellite galaxies. H I poor galaxies dominate the H I power spectrum of satellites. At small scales, we have noted the role of 'orphan galaxies' (i.e. galaxies whose parent dark matter substructure has been stripped below the resolution of the simulation): these peculiar satellites populate the most central regions of haloes and contribute to the total H I clustering. The importance of this contribution increases when lower resolution simulations are considered.

(iv) We have computed the H I power spectrum in redshift space, as the measurement of the 21 cm signal will map directly frequencies into redshifts. We have shown that the effect of peculiar velocities of galaxies produces the expected Kaiser effect at large scales, and the Finger-of-God reduction of power on the smaller scales. Moreover, as done in Villaescusa-Navarro et al. (2018), we have tested the agreement with linear theory, comparing the ratio of the power spectrum in redshift space and real space with the Kaiser limit (see equation 9). We have shown that, at redshift $z \gtrsim 4$, linear theory works up to $k \sim 0.4 \, h \, \mathrm{Mpc}^{-1}$;

Our model predictions are consistent with results from the Illustris simulation, described in Villaescusa-Navarro et al. (2018). The shot-noise levels are consistent within a factor of two, although we predict a steadily decreasing shot noise with redshift, while Villaescusa-Navarro et al. (2018) find that the shot noise decreases only for $z \geq 1$. Interestingly, Baugh et al. (2019) find a completely different behaviour: their shot-noise level increases with redshift. Villaescusa-Navarro et al. (2018) show that, at low redshift, H I-poor haloes are more clustered than H I-rich haloes: this agrees with our discussion on the red and blue galaxy population. Moreover, our H I bias values are consistent with their results. The H I bias stays roughly constant also on the largest scales that we can probe with the MI simulation, as expected for theoretical predictions. From $z = 1$ to $z = 2$, we find a constant $b_{\mathrm{H I}}$ up to $k \sim 2h \, \mathrm{Mpc}^{-1}$ while, at higher redshift, a scale dependence is already noticeable at $k \sim 0.3h \, \mathrm{Mpc}^{-1}$, again in agreement with Villaescusa-Navarro et al. (2018). The dip at $k \sim 1h \, \mathrm{Mpc}^{-1}$ at $z = 0$ is present also in the Illustris simulation. This feature is not present in the results of Baugh et al. (2019) since it is linked to the one-halo term, while they are computing the H I power spectrum placing the entire H I content of each halo at its centre of mass. Villaescusa-Navarro et al. (2018) demonstrated that the one-halo term is important to have a proper description of the signal, especially in redshift space. Indeed, HOD techniques will need to incorporate prescriptions for the H I distribution inside haloes. Our results on of the role of satellites on small scales constitutes a step in this direction. Finally, using the power spectrum in redshift space, we have computed the resulting 21 cm signal in mK^2, as a function of redshift. Our results depend on the evolution of the value of the H I neutral fraction $x_{\mathrm{H I}}$ and of the H I distribution across time. Future IM data from the SKA radio telescope and its pathfinders will allow us to test these predictions. On the other hand, the flexibility of SAMs will be crucial to interpret these data. The feedback process between data and galaxy evolution models will greatly enrich our understanding of the Universe and our capability to forecast and constrain cosmological scenarios.

REFERENCES

Anderson C. J. et al., 2018, MNRAS, 476, 3382
Ando R., Nishizawa A. J., Hasegawa K., Shimizu I., Nagamine K., 2019, MNRAS, 484, 5389
Bacon D. J. et al., 2020, Publ. Astron. Soc. Aust., 37, E007
Bagla J. S., Khandai N., Datta K. K., 2010, MNRAS, 407, 567
Baldry I. K. et al., 2012, MNRAS, 421, 621
Ballardini M., Finelli F., Maartens R., Moscardini L., 2018, J. Cosmol. Astropart. Phys., 2018, 044
Bandura K. et al., 2014, in Hall H. J., Gilmozzi R., Marshall H. K., eds, Proc. SPIE Conf. Ser. Vol. 9145, Ground-Based and Airborne Telescopes V. SPIE, Bellingham, p. 914522
Barnes L. A., Haehnelt M. G., 2010, MNRAS, 403, 870
Battye R. A., Davies R. D., Weller J., 2004, MNRAS, 355, 1339
Baugh C. M. et al., 2019, MNRAS, 483, 4922
Berry M., Somerville R. S., Haas M. R., Gawiser E., Maller A., Popping G., Trager S. C., 2014, MNRAS, 441, 939
Bharadwaj S., Nath B. B., Sethi S. K., 2001, J. Astrophys. Astron., 22, 21
Blitz L., Rosolowsky E., 2006, ApJ, 650, 933
Boylan-Kolchin M., Springel V., White S. D. M., Jenkins A., Lemson G., 2009, MNRAS, 398, 1150
Breysse P. C., Anderson C. J., Berger P., 2019, Phys. Rev. Lett., 123, 231105
Bull P., Ferreira P. G., Patel P., Santos M. G., 2015, ApJ, 803, 21
Camera S., Santos M. G., Ferreira P. G., Ferramacho L., 2013, Phys. Rev. Lett., 111, 171302
Carucci I. P., Villaescusa-Navarro F., Viel M., Lapi A., 2015, J. Cosmol. Astropart. Phys., 2015, 047
Castorina E., Villaescusa-Navarro F., 2017, MNRAS, 471, 1788
Chang T.-C., Pen U.-L., Peterson J. B., McDonald P., 2008, Phys. Rev. Lett., 100, 091303
Chang T.-C., Pen U.-L., Bandura K., Peterson J., 2010, Nature, 466, 51
Cooray A., 2006, Phys. Rev. Lett., 97, 261301
Cora S. A. et al., 2018, MNRAS, 479, 2
Cox T. J., Jonsson P., Somerville R. S., Primack J. R., Dekel A., 2008, MNRAS, 384, 386
Crighton N. H. M. et al., 2015, MNRAS, 452, 217
Croton D. J. et al., 2006, MNRAS, 365, 11
Davé R., Katz N., Oppenheimer B. D., Kollmeier J. A., Weinberg D. H., 2013, MNRAS, 434, 2645
Davé R., Rafieferantsoa M. H., Thompson R. J., Hopkins P. F., 2017, MNRAS, 467, 115
De Lucia G., Blaizot J., 2007, MNRAS, 375, 2
De Lucia G., Boylan-Kolchin M., Benson A. J., Fontanot F., Monaco P., 2010, MNRAS, 406, 1533
De Lucia G., Tornatore L., Frenk C. S., Helmi A., Navarro J. F., White S. D. M., 2014, MNRAS, 445, 970
Diemer B. et al., 2018, ApJS, 238, 33
Duffy A. R., Kay S. T., Battye R. A., Booth C. M., Dalla Vecchia C., Schaye J., 2012, MNRAS, 420, 2799
Fu J., Guo Q., Kauffmann G., Krumholz M. R., 2010, MNRAS, 409, 515
Furlanetto S. R., Oh S. P., Briggs F. H., 2006, Phys. Rep., 433, 181
Gao L., White S. D. M., 2007, MNRAS, 377, L5
Gao L., De Lucia G., White S. D. M., Jenkins A., 2004a, MNRAS, 352, L1
Gao L., White S. D. M., Jenkins A., Stoehr F., Springel V., 2004b, MNRAS, 355, 819
Giovanelli R. et al., 2005, AJ, 130, 2598
Gnedin N. Y., 2000, ApJ, 542, 535
Gonzalez-Perez V. et al., 2017, MNRAS, 474
Guha Sarkar T., Mitra S., Majumdar S., Choudhury T. R., 2012, MNRAS, 421, 3570

Guo Q., White S., Angulo R. E., Henriques B., Lemson G., Boylan-Kolchin M., Thomas P., Short C., 2013, MNRAS, 428, 1351

Henriques B. M. B., White S. D. M., Thomas P. A., Angulo R. E., Guo Q., Lemson G., Springel V., 2013, MNRAS, 431, 3373

Hirschmann M., De Lucia G., Fontanot F., 2016, MNRAS, 461, 1760

Kaiser N., 1987, MNRAS, 227, 1

Kennicutt Jr. R. C. et al., 2007, ApJ, 671, 333

Kim H.-S., Baugh C. M., Benson A. J., Cole S., Frenk C. S., Lacey C. G., Power C., Schneider M., 2011, MNRAS, 414, 2367

Kim H.-S., Wyithe J. S. B., Power C., Park J., Lagos C. d. P., Baugh C. M., 2015, MNRAS, 453, 2315

Kim H.-S., Wyithe J. S. B., Baugh C. M., Lagos C. d. P., Power C., Park J., 2017, MNRAS, 465, 111

Lagos C. d. P., Baugh C. M., Lacey C. G., Benson A. J., Kim H.-S., Power C., 2011, MNRAS, 418, 1649

Lagos C. d. P., Baugh C. M., Zwaan M. A., Lacey C. G., Gonzalez-Perez V., Power C., Swinbank A. M., van Kampen E., 2014, MNRAS, 440, 920

Lagos C. d. P. et al., 2015, MNRAS, 452, 3815

Leroy A. K., Walter F., Brinks E., Bigiel F., de Blok W. J. G., Madore B., Thornley M. D., 2008, AJ, 136, 2782

Loeb A., Wyithe J. S. B., 2008, Phys. Rev. Lett., 100, 161301

Majumdar S., Pritchard J. R., Mondal R., Watkinson C. A., Bharadwaj S., Mellema G., 2018, MNRAS, 476, 4007

Mancuso C. et al., 2017, ApJ, 842, 95

Marín F. A., Gnedin N. Y., Seo H.-J., Vallinotto A., 2010, ApJ, 718, 972

Martin A. M., Papastergis E., Giovanelli R., Haynes M. P., Springob C. M., Stierwalt S., 2010, ApJ, 723, 1359

Masui K. W. et al., 2013, ApJ, 763, L20

Meyer M. J. et al., 2004, MNRAS, 350, 1195

Monaco P., Theuns T., Taffoni G., 2002, MNRAS, 331, 587

Moustakas J. et al., 2013, ApJ, 767, 50

Newburgh L. B. et al., 2016, in Hall H. J., Gilmozzi R., Marshall H. K., eds, Proc. SPIE Conf. Ser. Vol. 9906, Ground-Based and Airborne Telescopes VI. SPIE, Bellingham, p. 99065X

Obuljen A., Alonso D., Villaescusa-Navarro F., Yoon I., Jones M., 2019, MNRAS, 486, 1075

Padmanabhan H., Refregier A., Amara A., 2017, MNRAS, 469, 2323

Pénin A., Umeh O., Santos M. G., 2018, MNRAS, 473, 4297

Pillepich A., Porciani C., Matarrese S., 2007, ApJ, 662, 1

Planck Collaboration XIII, 2016, A&A, 594, A13

Planck Collaboration VI, 2018, preprint (arXiv:1807.06209)

Pontzen A. et al., 2008, MNRAS, 390, 1349

Popping G., Somerville R. S., Trager S. C., 2014, MNRAS, 442, 2398

Popping G. et al., 2015, MNRAS, 454, 2258

Pritchard J., Loeb A., 2010, Nature, 468, 772

Rahmati A., Pawlik A. H., Raičević M., Schaye J., 2013, MNRAS, 430, 2427

Santos M. et al., 2015, Proc. Sci., Advancing Astrophysics with the Square Kilometre Array (AASKA14). SISSA, Trieste, PoS#19

Santos M. G. et al., 2017, preprint (arXiv:1709.06099)

Sarkar D., Majumdar S., Bharadwaj S., 2019, MNRAS, 490, 2880

Sefusatti E., Crocce M., Scoccimarro R., Couchman H. M. P., 2016, MNRAS, 460, 3624

Sheth R. K., Tormen G., 1999, MNRAS, 308, 119

Somerville R. S., Davé R., 2015, ARA&A, 53, 51

Somerville R. S., Primack J. R., Faber S. M., 2001, MNRAS, 320, 504

Spergel D. N. et al., 2003, ApJS, 148, 175

Springel V., White S. D. M., Tormen G., Kauffmann G., 2001, MNRAS, 328, 726

Springel V. et al., 2005, Nature, 435, 629

Stevens A. R. H., Lagos C. d. P., Contreras S., Croton D. J., Padilla N. D., Schaller M., Schaye J., Theuns T., 2017, MNRAS, 467, 2066

Switzer E. R. et al., 2013, MNRAS, 434, L46

Tescari E., Viel M., Tornatore L., Borgani S., 2009, MNRAS, 397, 411

Villaescusa-Navarro F., Viel M., Datta K. K., Choudhury T. R., 2014, J. Cosmol. Astropart. Phys., 2014, 050

Villaescusa-Navarro F., Bull P., Viel M., 2015, ApJ, 814, 146

Villaescusa-Navarro F., Alonso D., Viel M., 2017, MNRAS, 466, 2736

Villaescusa-Navarro F. et al., 2018, ApJ, 866, 135

Wang J., De Lucia G., Kitzbichler M. G., White S. D. M., 2008, MNRAS, 384, 1301

Wong T., Blitz L., 2002, ApJ, 569, 157

Wyithe J. S. B., Brown M. J. I., 2010, MNRAS, 404, 876

Xie L., De Lucia G., Hirschmann M., Fontanot F., Zoldan A., 2017, MNRAS, 469, 968

Xu Y., Wang X., Chen X., 2015, ApJ, 798, 40

Xu Y., Hamann J., Chen X., 2016, Phys. Rev. D, 94, 123518

Zavala J. et al., 2016, MNRAS, 460, 4466

Zoldan A., De Lucia G., Xie L., Fontanot F., Hirschmann M., 2017, MNRAS, 465, 2236

Zwaan M. A., Meyer M. J., Staveley-Smith L., Webster R. L., 2005, MNRAS, 359, L30

APPENDIX A: CONDITIONAL H I MASS FUNCTION AT HIGH REDSHIFT

In this appendix, we extend the analysis of Section 3.1 to higher redshift. In Fig. A1, we show the H I mass function at $z = 4$ for MI and MII (right-hand and left-hand panels, respectively). We show the H I mass function for all the galaxies in the top panels, for the central galaxies in the middle panels, and the satellite galaxies in the bottom panels. We further divide model galaxies according to their halo mass (see legend). At $z = 4$, we find very few galaxies with $M_{HI} \gtrsim 10^{10}\,M_\odot$, and also very massive haloes ($M_h > 10^{14}\,h^{-1}\,M_\odot$) are not yet formed. Despite these differences, the global relative contributions of haloes of different masses to the H I mass functions is similar to what found at $z = 0$ (see Fig. 2), especially for central galaxies. In the case of satellite galaxies, we notice a swap in the relative importance of haloes of mass $10^{12} < M_h[h^{-1}\,M_\odot] < 10^{14}$ and $10^{10} < M_h[h^{-1}\,M_\odot] < 10^{12}$, most likely due to the hierarchical growth of structures.
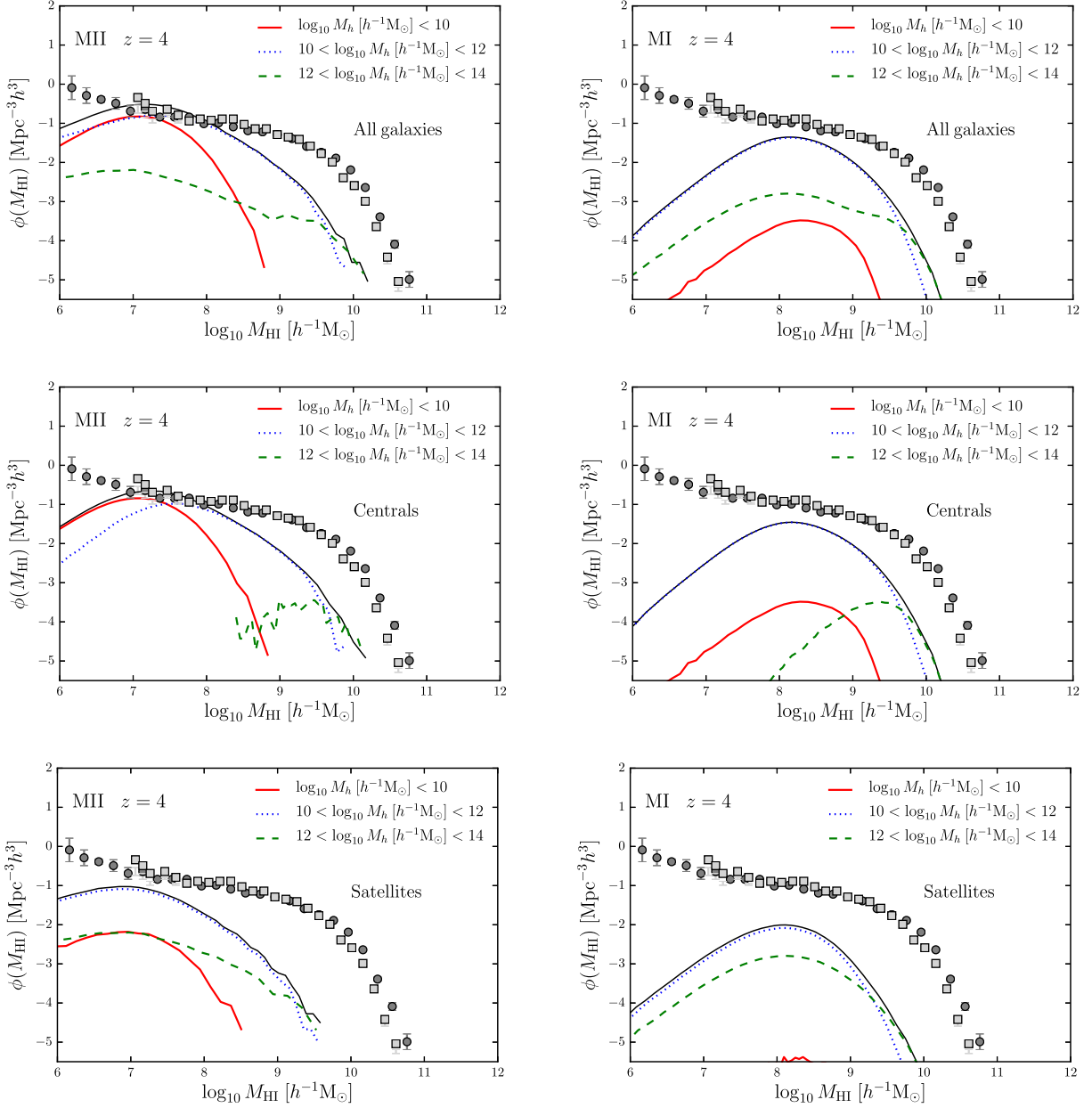
Figure A1. The predicted H I conditional mass function for the MII (left column) and the MI (right column) at $z = 4$. In the middle and bottom panels, we separate the contribution from central and satellite galaxies, respectively. The solid black line in each panel is the sum of the contributions from different host dark matter haloes. To better appreciate the difference with $z = 0$, we add with squares and circles the data measured by Zwaan et al. (2005) and Martin et al. (2010), the blind H I surveys HIPASS (Meyer et al. 2004) and ALFALFA (Giovanelli et al. 2005) in the local Universe.

APPENDIX B: H I HALO MASS FUNCTION: FITTING FORMULAE

With the aim of extracting from SAMs the properties that can be useful for HOD techniques to simulate 21 cm maps for IM, we extend, in this appendix, the analysis of Section 5.1. In particular, we model the H I halo mass function $M_{H I}(M_h)$ dividing central and satellite galaxies (see Fig. 7). For central galaxies we use the same formula as for the total, i.e. equation (2) and report the best-fitting values of the parameter in Table B1. As redshift increases, we can see that M_{break} increases, as can also be seen in Fig. 7. The low values for M_{min} also at redshift zero indicate that the low-mass cut-off is mainly driven by satellites. For the case of satellites, we use

Table B1. Best-fitting values for the parameters of the H I halo mass function $M_{H I}(M_h)$ of equation (2) as a function of redshift when only centrals are considered (see Fig. 7). The cut-off parameter γ is fixed here to 0.5 as for the total H I halo mass function.

z	a_1	a_2	α	β	$\log_{10}(M_{break})$ $(h^{-1} M_\odot)$	$\log_{10}(M_{min})$ $(h^{-1} M_\odot)$
0	2.9e−3	6.8e−5	0.41	0.85	10.66	−1.98
1	1.6e−3	1.1e−4	0.56	0.43	11.86	−2.99
2	1.3e−3	4.5e−4	0.74	0.25	12.26	−3.01
3	2.2e−3	−2.3e−4	0.46	0.15	12.27	−3.75
4	3.3e−3	−1.1e−3	0.35	0.12	12.28	−3.90
5	3.9e−3	−1.5e−3	0.30	0.10	12.10	−3.01

Table B2. Best-fitting values for the parameters of the H I halo mass function $M_{HI}(M_h)$ of equation (B1) as a function of redshift when only satellites are considered (see Fig. 7).

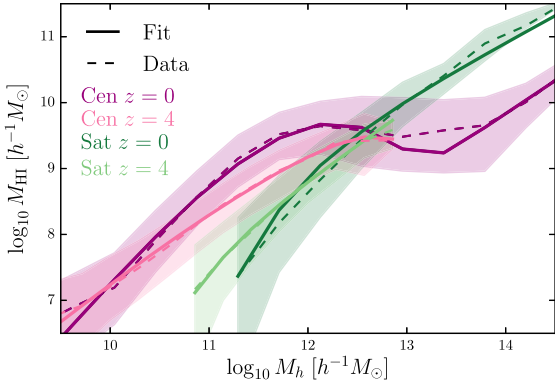| z	$\log_{10}(M_0)$ $(h^{-1}\,M_\odot)$	$\log_{10}(M_{min})$ $(h^{-1}\,M_\odot)$	α	γ
0	9.30	12.0	0.81	0.70
1	8.31	11.4	1.10	0.84
2	7.66	11.00	1.16	1.05
3	7.23	10.75	1.22	1.44
4	7.74	10.95	1.05	0.90
5	7.11	10.63	1.20	1.83

Figure B1. Comparison between the data (dashed lines) and the best fits of Tables B1 and B2 (solid lines) shown for both centrals (in magenta) and satellites (in green), for two different redshifts ($z = 0$ and $z = 4$), with the same colour code of Fig. 7. Shaded regions indicate the 16–84 percentile of the data.

Table B3. Best-fitting values for the parameters of the H I halo mass function $M_{HI}(M_h)$ of equation (2) at $z = 0$, as a function of assembly time (see Fig. 8). These value are obtained with a fixed value of the parameter $\gamma = 0.3$.

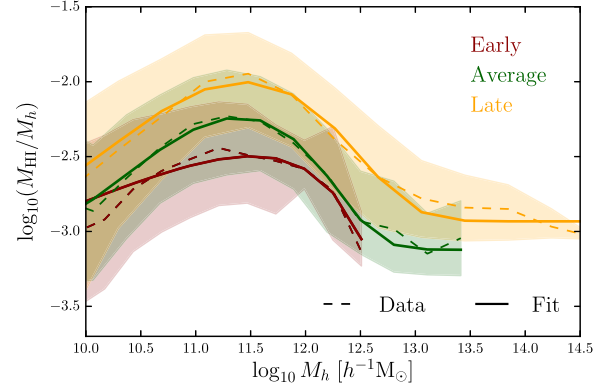| z_{50}	a_1	a_2	α	β	$\log_{10}(M_{break})$ $(h^{-1}\,M_\odot)$	$\log_{10}(M_{min})$ $(h^{-1}\,M_\odot)$
Early	1.6e−3	−5.4e−5	0.80	0.29	12.06	−7.82
Average	2.0e−3	7.5e−4	0.39	1.35	10.02	−5.46
Late	2.5e−2	1.2e−03	0.25	1.60	8.24	−3.89

Figure B2. Comparison between the data (dashed lines) and the best fits of Table B3 (solid lines) shown for the three cases early, average and late assembly, with the same colour code of Fig. 8. Shaded regions indicate the 16–84 percentile of the data.

the standard formula (e.g. Castorina & Villaescusa-Navarro 2017; Padmanabhan et al. 2017; Villaescusa-Navarro et al. 2018; Obuljen et al. 2019)

$$M_{HI}(M_h) = M_0 \left(\frac{M}{M_{min}} \right)^\alpha e^{-\left(\frac{M_{min}}{M_h} \right)^\gamma}, \qquad (B1)$$

where M_0, M_{min}, α, and γ are the fitted parameters. The best-fitting values are reported in Table B2. We show in Fig. B1 the qualitatively agreement between the model and the data for both centrals and satellites, choosing two representative redshifts, $z = 0$ and $z = 4$.

We analyse also the dependence on assembly bias (see Fig. 8). As described in Section 5.1, we use as a proxy for assembly history the redshift at which a halo has acquired half of its final mass, i.e. z_{50}. We define 'young/late' assembled haloes as those whose z_{50} falls within the 33th percentile of the distribution, 'average age' haloes as those whose z_{50} is within the 33th and the 66th percentiles and 'old/early' assembly haloes as those whose z_{50} ranges above the 66th percentile. The 33th and 66th percentile are computed globally and correspond to redshift of 1.6 and 2.4, respectively. In Table B3, we report the fitting formula for the three cases. We use again equation (2), fixing $\gamma = 0.3$. In Fig. B2, we show the qualitatively agreement between the model and the data. As discussed in Section 5.1, the dependence on assembly history is related to the scatter of the $M_{HI}(M_h)$ relation. To illustrate the scatter, in Fig. B3, we show the H I halo mass function at redshift $z = 0$ and $z = 4$, colour coded with the number of haloes in each bin, for both the MII and the MI. The figure allows also to appreciate the agreement between the data and the best fit of Table 2. We show only the cases $z = 0$ and $z = 4$, but the agreement is similar at all redshifts.
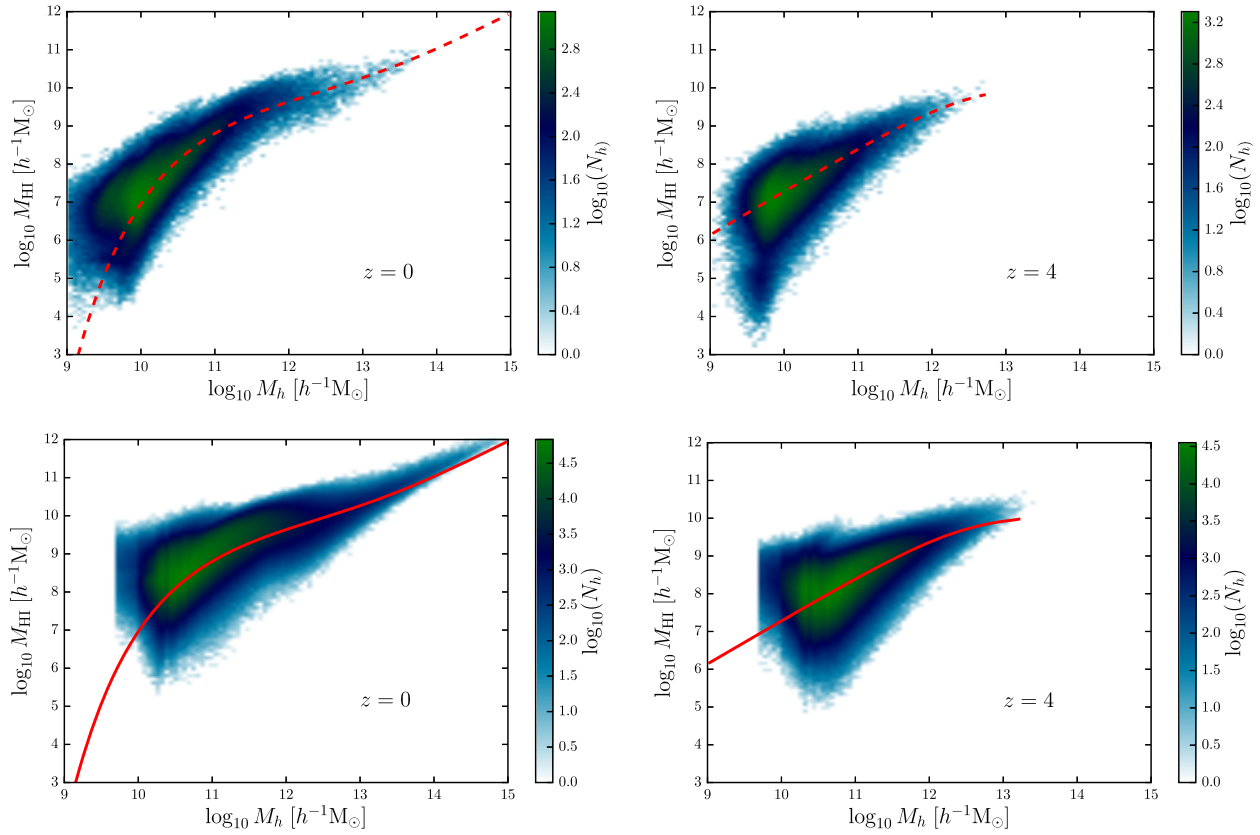
Figure B3. The predicted H I halo mass function $M_{\mathrm{H1}}(M_{\mathrm{h}})$ at redshift $z = 0$ and redshift $z = 4$, colour coded by the number of haloes in each bin. The red lines show the best-fitting values of Table 2 obtained with the parametrization given in equation 2. *Top panels*: MII. *Bottom panels:* MI. Note that the best-fitting value reported here is the one from the MII case, to show the agreement between the two simulations.

This paper has been typeset from a TEX/LATEX file prepared by the author.